

# Effects of surface wettability and flow rates on the interface evolution and droplet pinch-off mechanism in the cross-flow microfluidic systems

Akepogu Venkateshwarlu<sup>a</sup>, Ram Prakash Bharti<sup>a,\*</sup>

<sup>a</sup>Complex Fluid Dynamics and Microfluidics (CFDM) Lab, Department of Chemical Engineering, Indian Institute of Technology Roorkee, Roorkee - 247667, Uttarakhand, INDIA

---

## Abstract

In this study, the effect of surface wettability on the two-phase immiscible fluids flow and dynamics of droplet pinch-off in a T-junction microchannel has been numerically investigated using the finite element method. A conservative level set method (CLSM) has been adopted to capture the interface topology in the squeezing regime ( $Ca_c < 10^{-2}$ ) for wide flow rate ratio ( $1/10 \leq Q_r \leq 10$ ) and contact angle ( $120^\circ \leq \theta \leq 180^\circ$ ). This study has revealed that the wettability is a dominant factor in determining the hydrodynamic features of the droplet. Based on the instantaneous phase flow profiles, the droplet formation stages are classified as: initial, filling, squeezing, pinch-off and stable droplet. Wettability effects are insignificant in the filling stage. However, the hydrophobic effects are more vital in the squeezing and pinch-off stages. In general, it is shown that engineering parameters have complex dependence on the dimensionless parameters ( $Ca_c$ ,  $Q_r$ ,  $\theta$ ). Capturing the instantaneous interface evolution has revealed that the droplet shape is sensitive to the contact angle. Interface shape profiles transform from convex into concave immediately for hydrophobic conditions ( $120^\circ \leq \theta \leq 150^\circ$ ) whereas slowly for the super hydrophobic conditions ( $150^\circ < \theta \leq 180^\circ$ ). In contrast to the literature, the pressure in the dispersed phase is not constant, but it is an anti-phase with the pressure in the continuous phase. Maximum pressure in the continuous phase, and neck width of the interface are complex function of the governing conditions ( $Ca_c$ ,  $Q_r$ ,  $\theta$ ). Comparison of the filling and pinch-off time based on the pressure and phase profiles has brought new insights that the droplet pinch-off mechanism can be elucidated by installing the pressure sensors even without the flow visualization and phase profiles. The interface curvature adopts a flattened to a more concave shape when the Laplace pressure varies from a smaller to higher value. The interface neck width ( $2r$ ) shows an increasing trend up to a threshold value and then decreases linearly with the contact angle.

**Keywords:** Droplets, Microfluidics, Droplet pinch-off, Wettability, CFD, Interface evolution, Level set method, Laplace pressure

---

\*Corresponding author.

Email address: rpbharti@iitr.ac.in (Ram Prakash Bharti)

# 1. INTRODUCTION

Microfluidics has become an emerging field in the contemporary research world due to its versatile applications. It has triggered technological revolutions in interdisciplinary engineering, science, biochemical and biomedical like emulsions, mixing reactions, diagnostics, protein encapsulation, DNA analysis, new material synthesis, paints, inks, and coating ([Barnes, 1994](#); [Abate et al., 2013](#); [Wu et al., 2014](#); [Hou et al., 2017](#); [Kaminski and Garstecki, 2017](#); [Boruah et al., 2018](#); [Weng and Spoonamore, 2019](#); [Schroen et al., 2021](#); [Bharti and Gangawane, 2022](#); [Jung et al., 2022](#)). Microfluidic devices are frequently applied as a potential platform to generate droplet emulsions by using various geometric configurations and methods. Commonly used microfluidic devices to generate the droplets are co-flow, cross-flow, and flow-focusing devices ([Carrier et al., 2014](#); [Moon et al., 2014](#)). Amongst others, T-junction cross-flow microfluidic device (Figure 1a) is prevalent for producing monodispersed droplets due to its simplicity and ease of controlling the generation ([Venkateshwarlu and Bharti, 2021, 2022b,a](#)). The displacement of the dispersed phase and formation of the droplet through the microchannels is governed mainly by important determinants like capillary number (ratio of viscous to interfacial tension forces), and Reynolds number (ratio of inertial to viscous forces) ([Mastiani et al., 2017](#); [Agarwal et al., 2020](#); [Venkateshwarlu and Bharti, 2021, 2022b,a](#)).

The dynamic behavior of the droplet generation is governed by the three fundamental characteristics which express the exerting surface forces: (a) contact angle - described by the surface energies where they meet; (b) pressure jump across the surfaces and interfaces - higher pressure on the concave side of the surface, and (c) the shear stress caused by the surface tension gradient - the pressure difference between each side of the interface is caused by the surface tension; the pressure essentially causes the bulge, and hence it is always higher on the concave side of the interface ([Trefethen, 1969](#); [Bashir et al., 2014](#); [Shi et al., 2014](#); [Venkateshwarlu and Bharti, 2022b](#)).

Surface wettability, i.e., fluid-solid interaction (FSI), is known to play a vital role in many

physical, chemical, biological, and industrial processes related to agriculture (efficiency of pesticides), medicine (integration of implants with bone), food packaging (prolonged release of antimicrobial agents and increased shelf life), painting and printing (ensured suitable adhesion of liquid to solid), heat transfer and lubrication (consideration of surface energy), and oil recovery (selective absorption of oil in solid materials) (Huhtamaki et al., 2018). Surface wettability influences the degree of contact with the fluidic environment and is quantified in terms of the contact (or wetting) angle, inversely proportional to the surface energy. The contact angle ( $\theta$ , degrees) is defined geometrically as the angle between the tangent to the liquid-liquid interface and the solid surface at the three-phase (liquid-vapor/gas-solid or liquid-liquid-solid) contact line (Figure 1b). The interfacial tensions of solid-liquid ( $\sigma_{sl}$ ), solid-vapor ( $\sigma_{sv}$ ), and liquid-liquid ( $\sigma$ ) form the equilibrium contact angle of wetting ( $\theta$ ) (Figure 1b). It represents the strength of FSI (fluid-solid interaction) and is measured conventionally from the liquid (dispersed or heavier) side. For example, high surface energy (i.e., high  $\sigma_{sv}$ ) would exhibit a low  $\theta$  and the liquid tendency to spread and adhere to the surface. In contrast, low surface energy (i.e., low  $\sigma_{sl}$ ) demonstrates high  $\theta$  and the surface tendency to repel the liquid. The hydrophilicity diminishes<sup>1</sup> with increasing contact angle (Law, 2014). The contact angle between the ideal solid surface (i.e., atomically smooth, non-reactive, chemically homogeneous, and perfectly rigid) and liquid is defined by the well-known Young equation ( $\sigma_{sv} = \sigma_{sl} + \sigma \cos \theta$ ).

The surface wettability plays a significant role in droplet evolution. The contact angle greatly influences the droplet dynamics as it is affected by surface roughness, impurities on the solid surface, porosity, surface energy, and functional groups present on the surface (Boruah et al., 2018; Deka et al., 2022). The microfluidic devices are easier to control and manipulate as they do not require any secondary fluid to trigger the formation of the droplet, and the minimum contact angle of about  $\theta = 120^\circ$  is needed to form a droplet (Kawakatsu et al., 2001;

---

<sup>1</sup> $\theta = 0^\circ$ : perfect wetting (or super-hydrophilic);  $0^\circ < \theta < 90^\circ$ : spreading (or wettable or hydrophilic);  $\theta = 90^\circ$ : neutral ( $\sigma_{sl} = \sigma_{sv}$ , i.e., equal cohesive and adhesive forces);  $90^\circ < \theta < 180^\circ$ : repelling (or non-wettable or hydrophobic);  $\theta = 180^\circ$ : completely liquid-repellent (or non-wetting or super-hydrophobic).

[Maan et al., 2013](#); [Eggersdorfer et al., 2018](#)). The mono-dispersed droplets are generated by operating a T-junction microchannel under a squeezing or dripping regime. The geometry confinement suppresses the capillary instabilities; hence, the produced droplets are regular and stable ([van Steijn et al., 2007](#); [Glawdel et al., 2012](#); [Venkateshwarlu and Bharti, 2021, 2022b](#)).

Extensive literature is available on the dynamics of droplet generation through the cross-flow microfluidic systems ([Thorsen et al., 2001](#); [Nisisako et al., 2002](#); [Garstecki et al., 2006](#); [De menezes et al., 2008](#); [Christopher et al., 2008](#); [Gupta et al., 2009](#); [Wong et al., 2017](#); [Venkateshwarlu and Bharti, 2021, 2022b,a](#); [Dhondi et al., 2022](#); [Samadder et al., 2022](#); [Bharti and Gangawane, 2022](#)). The droplet formation process is divided into three stages (filling, squeezing, and instant pinch-off). The breakup (or pinch-off) step is, essentially, initiated by the pressure developed due to the reverse flow in the gutters between the channel wall and liquid-liquid interface (LLI). Further, the hydrodynamic pressure becomes equal on both sides of the interface at the pinch-off. The linear relationship predicts the dependence of the droplet size on the flow rate ratio in the squeezing flow regime ([van Steijn et al., 2009](#); [Glawdel et al., 2012](#); [Venkateshwarlu and Bharti, 2021](#)). Limited efforts ([van der Graaf et al., 2006](#); [Bashir et al., 2014](#); [Shi et al., 2014](#); [Boruah et al., 2018](#)) are also made to explore the influence of surface wettability on the dynamics of droplet generation in the microchannel. Although several attempts have been made to elucidate the droplet pinch-off mechanism by exploiting the interface curvature but still lacks to understand the effect of the contact angle on the interface curvature and the esoteric reason behind the shape evolution ([Wang et al., 2020](#)).

The main challenges in an in-depth study of the droplet pinch-off mechanisms are complexity in capturing the topological changes of the interface curvature and non-linearity of the equations. In addition, a detailed understanding of the mechanisms requires rigorous and precise post-processing and analysis of the results. Further, a detailed systematic study depicting the wettability effects on the interface evolution and droplet breakup mechanisms will be instrumental in controlling droplet-based phenomena of mixing, dispersion, paints, and

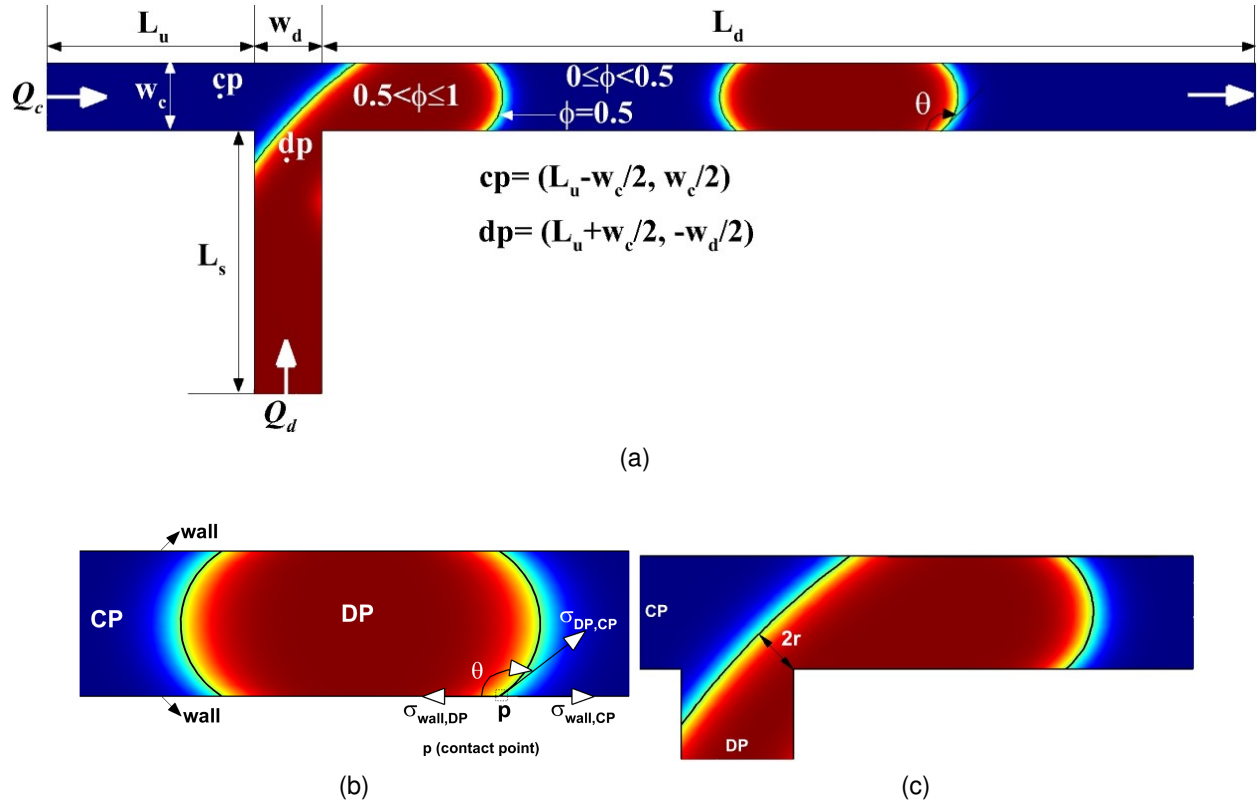


Figure 1: Schematic representation of (a) the two-phase flow in T-junction microfluidic device, (b) contact angle ( $\theta$ ), and (c) neck thickness of the interface ( $2r$ ).

coatings. Therefore, the present work aims to explore the influences of surface wettability on the dynamics of the interface evolution and droplet generation in cross-flow microfluidic devices.

## 2. PHYSICAL AND MATHEMATICAL MODELLING

Consider the two-dimensional laminar flow of two immiscible fluids through a cross-flow rectangular slit-type microfluidic system, as illustrated in Figure 1a. The microfluidic system depicts a T-junction by geometrically arranging a side (or vertical) channel perpendicularly to the horizontal main (or primary) channel. The geometrical dimensions (length, width) of the primary and side channels are  $(L_m, w_c)$  and  $(L_s, w_d)$ , respectively. The upstream length (i.e., the distance between the inlet of the primary channel and the front of the side channel) and

downstream length (i.e., the distance between the rear of the side channel and the outlet of the primary channel) are  $L_u$  and  $L_d$ , respectively. The length of the primary channel ( $L_m = L_u + w_d + L_d$ ) is taken to be sufficient to avoid the end effects. All the length quantities ( $L, w$ ) are measured in microns ( $\mu\text{m}$ ).

Both fluids are assumed to be Newtonian (i.e., constant viscosity,  $\mu$  Pa.s), isothermal (i.e., constant temperature,  $T$  °C), non-reactive, and incompressible (i.e., constant density,  $\rho$  kg/m<sup>3</sup>). The Marangoni and dynamic interfacial effects are ignored, and hence, the surface tension ( $\sigma$  N/m) is uniform throughout the device. Further, the device walls are considered to be ideal solid surfaces (i.e., atomically smooth, non-reactive, chemically homogeneous, and perfectly rigid).

The continuous phase (CP, indicated by blue color) and dispersed phase (DP, indicated by red color) enter (refer Figure 1a) from the inlets of the primary and side channels, with the fixed volumetric flow rates ( $\mu\text{l}/\text{min}$ ) of  $Q_c$  and  $Q_d$ , respectively. Both phases interact at the T-junction point, flow downstream, and exit through the primary channel open to the atmosphere (i.e.,  $p = 0$ ). Further, the flow is confined within the no-slip walls.

The above-stated physical problem is mathematically expressed by the conservation equations of mass (Eq. 1), momentum (Eq. 2), and phases (Eq. 6), as follows.

$$\nabla \cdot \mathbf{u} = 0 \quad (1)$$

$$\rho \left[ \frac{\partial \mathbf{u}}{\partial t} + \mathbf{u} \cdot \nabla \mathbf{u} \right] = -\nabla p + \nabla \cdot \boldsymbol{\tau} + \mathbf{F}_\sigma \quad (2)$$

where  $\mathbf{u}$ ,  $p$ , and  $t$  are the velocity vector, pressure, and time, respectively. The deviatoric stress tensor ( $\boldsymbol{\tau}$ ) is defined as follows.

$$\boldsymbol{\tau} = 2\mu\mathbf{D} \quad (3)$$

where  $\mathbf{D}$  is the rate of deformation tensor. The physical properties ( $X = \rho$  and  $\mu$ ) of the two

fluid phases (CP and DP) at any point are expressed as follows.

$$X = X_c + (X_d - X_c)\phi \quad (4)$$

where, the level set function ( $\phi$ ) represents the liquid phase composition whose value varies between  $\phi = 0$  (for pure CP) and  $\phi = 1$  (for pure DP). The values of  $\phi < 0.5$ ,  $\phi = 0.5$  and  $\phi > 0.5$  indicate for the CP, liquid-liquid interface (LLI) and DP, respectively.

The interfacial tension force (IFT,  $\mathbf{F}_\sigma$ ) acting between the two immiscible liquids is given as follows by the continuum surface force (CSF) model (Brackbill et al., 1992).

$$\mathbf{F}_\sigma = \sigma\kappa\delta(\phi)\mathbf{n} \quad (5)$$

where

$$\delta(\phi) = 6|\nabla\phi|\phi(1-\phi), \quad \kappa = (1/R) = -(\nabla \cdot \mathbf{n}) \quad \text{and} \quad \mathbf{n} = \frac{\nabla\phi}{|\nabla\phi|}$$

where  $\sigma$ ,  $\mathbf{n}$ ,  $\delta$ ,  $\kappa$ , and  $R$  are the liquid-liquid surface tension coefficient (N/m), unit normal, the Dirac delta function approximated by a smooth function, mean curvature, and the radius of curvature, respectively.

The conservative level set method (CLSM) is well-suited to capture the topological changes of moving interfaces. It is a robust scheme that is relatively easy to implement (Osher and Sethian, 1988; Olsson and Kreiss, 2005; Akhlaghi Amiri and Hamouda, 2013; Gada and Sharma, 2009; Bashir et al., 2011; Wong et al., 2017). The following level set equation (LSE) expresses the conservation of the phase field.

$$\frac{\partial\phi}{\partial t} + \mathbf{u} \cdot \nabla\phi = \gamma\nabla \cdot [\epsilon_s \nabla\phi - \phi(1-\phi)\mathbf{n}] \quad (6)$$

The level set parameters  $\gamma$ , and  $\epsilon_s$  acts for the re-initialization and stabilization of  $\phi$ , and controlling interface thickness, respectively.

The physical boundary conditions for the governing equations (Eqs. 1 - 6) stated above are as follows.

- (a) Fixed flow rate of CP ( $Q_c \mu\text{l}/\text{min}$ ) at the inlet of the primary channel.
- (b) Fixed flow rate of DP ( $Q_d \mu\text{l}/\text{min}$ ) at the inlet of vertical channel.
- (c) Constant ambient pressure ( $p = 0$ ) and fully developed velocity and phase fields at the outlet of the primary channel.
- (d) The wetted wall boundary condition, which allows the fluid-fluid interface to move along the wall, has been imposed on all the no-slip solid walls. This condition requires a slip length ( $\beta \mu\text{m}$ ), i.e., the distance outside the solid surface at which the tangential component of the velocity extrapolated to zero (Bashir et al., 2011; Yan et al., 2012; Hernández-Cid et al., 2022). The value of  $\beta$  is generally equivalent to the local mesh size element ( $h \mu\text{m}$ ).

For laminar flow, the boundary condition for the wetted wall to enforce a no-penetration condition on the solid surface (wall) is  $\mathbf{u} \cdot \mathbf{n}_s = 0$ , where  $\mathbf{n}_s$  is a unit normal to the solid surface. The tangential stress is defined as  $\mathbf{F}_{\text{fr}} = -(\mu/\beta)\mathbf{u}$ . The boundary force to enforce the contact angle is defined as  $\mathbf{F}_\theta = \sigma\delta(\mathbf{n}_s \cdot \mathbf{n} - \cos \theta)\mathbf{n}$ , where  $\theta$  is the static contact angle ( $\theta_s$ ) between the solid wall and the fluid interface (Gerbeau and Lelièvre, 2009; Bashir et al., 2014; Mirzaaghaian et al., 2020; COMSOL, 2022). In weak form, the wetted wall boundary condition is expressed as:

$$\int_{\partial\Omega} \mathbf{u}_t \cdot [\sigma(\mathbf{n}_s - (\mathbf{n} \cos \theta_s))\delta] dS = 0 \quad (7)$$

where  $\mathbf{u}_t$  is the test function used in the Galerkin finite element method; it is a function of velocity ( $\mathbf{u}$ ) and domain ( $\partial\Omega$ ). The Lagrange multipliers are used to implement this condition in COMSOL by the Galerkin finite element approximation (variational approach).



Finally, it is appropriate to define the non-dimensional parameters used in the present work.

$$\begin{aligned} Re_c &= \frac{\rho_c u_c w_c}{\mu_c}, & Ca_c &= \frac{u_c \mu_c}{\sigma}, & Q_r &= \frac{Q_d}{Q_c}, & w_r &= \frac{w_d}{w_c}, \\ \rho_r &= \frac{\rho_d}{\rho_c}, & \mu_r &= \frac{\mu_d}{\mu_c}, & p &= p^* \left( \frac{w_c}{u_c \mu_c} \right), & t &= t^* \left( \frac{u_c}{w_c} \right), & 2r &= \frac{2r^*}{w_c} \end{aligned} \quad (8)$$

where  $Re$  and  $Ca$  are the Reynolds, and capillary numbers. The subscripts ‘r’, ‘c’, and ‘d’ denote for ratio, CP, and DP, respectively. The variables with asterisk (\*) superscript are dimensional, but denoted without asterisk (\*) before Eq. (8). Further, the neck width ( $2r$ ) is defined (Venkateshwarlu and Bharti, 2022b) as the shortest distance from the receding interface to the lower-right corner of the junction (refer Figure 1c).

The numerical solution of the mathematical model, subject to the boundary conditions, provides an instantaneous flow ( $\mathbf{u}$ ,  $p$ ) and phase ( $\phi$ ) fields as a function of dimensionless parameters ( $Re_c$ ,  $Ca_c$ ,  $Q_r$ ,  $w_r$ ,  $\rho_r$ ,  $\mu_r$ ). The post-processing of these fields is further performed to gain insights of the dynamics of interface development and droplet generation. The next section details the numerical modelling and governing parameters used in this work.

### 3. NUMERICAL MODELLING AND PARAMETERS

In this study, the computational fluid dynamics (CFD) simulations of the mathematical model have been performed using the finite element method (FEM) based COMSOL multiphysics for determining the phase ( $\phi$ ), velocity ( $\mathbf{u}$ ), and pressure ( $p$ ) fields. Since the detailed solution approach is presented in our recent studies (Venkateshwarlu and Bharti, 2021, 2022b), only salient features are included here. The present mathematical model is expressed in COMSOL by using the “two-dimensional (2-D) → fluid flow ( $ff$ ) → multiphase flow ( $mpf$ ) → two-phase flow, level set ( $tpfls$ ) → laminar flow ( $lf$ )” modules. The computational domain (Figure 1a) is discretized using 2-D, linear, non-uniform, unstructured, triangular mesh elements. The transient PDEs (partial differential equations) are transformed into ODE (ordinary differential equations) by using the finite element method (FEM). The spatial

interpolation of both pressure and velocity fields is performed using the shape functions of the first-order polynomial (i.e.,  $P_1+P_1$ ). Further, the temporal derivatives in ODEs have been discretized using an implicit backward differentiation formula (BDF). The accuracy of the solution is generally a trade-off with the stable convergence for the higher- to lower-order BDF approximation. The discretization process results in differential-algebraic equations (DAEs) with variable time steps ( $\Delta t$ ).

The fully converged numerical solution of DAEs have been obtained using a fully coupled Newton's non-linear and PARDISO solvers with a sufficiently low time step ( $\Delta t = 10 \mu\text{s}$ ) and the relative tolerance ( $5 \times 10^{-3}$ ) for the following ranges of conditions.

- Geometrical parameters:  $w_c = 100 \mu\text{m}$ ;  $w_r = 1$ ;  $L_u = L_s = 9w_c$ ;  $L_d = 30w_c$ ;  $L_m = 40w_c$
- Mesh parameters:  $N_e = 13766$ ; DoF = 53029;  $h_{\text{max}} = 10 \mu\text{m}$
- Level set parameters:  $\gamma = 1 \text{ m/s}$ ;  $\epsilon_{\text{ls}} = h_{\text{max}}/2$
- Fluid and flow parameters:  $Ca_c < 10^{-2}$ ;  $Re_c = 0.1$ ;  $120^\circ \leq \theta \leq 180^\circ$ ;  $0.1 \leq Q_r \leq 10$ ;  $Q_d = 0.14 \mu\text{l/s}$ ;  $\rho_d = 1000 \text{ kg/m}^3$ ;  $\mu_d = 0.001 \text{ Pa}\cdot\text{s}$ ;  $7.143 \times 10^{-3} \leq \mu_r \leq 7.143 \times 10^{-1}$ ;  $1.96 \times 10^{-6} \leq \sigma \leq 1.96 \times 10^2 \text{ N/m}$

The above noted geometrical, mesh and simulation parameters have been tested in our recent study ([Venkateshwarlu and Bharti, 2021](#)) for their dependence on the numerical results.

## 4. RESULTS AND DISCUSSION

In this section, the effects of surface wettability ( $120^\circ \leq \theta \leq 180^\circ$ ) and the flow rate ratio ( $0.1 \leq Q_r \leq 10$ ) on the instantaneous evolution of the interface and the droplet pinch-off mechanism have been elucidated through an instantaneous phase ( $\phi$ ) and pressure ( $p$ ) evolutions, neck thickness or width ( $2r$ ), and the Laplace pressure ( $p_L$ ) acting on the interface for the broad conditions of the microfluidic flow. It is noted here the results for the droplet pinch-off dynamics

for a fixed contact angle ( $\theta = 135^\circ$ ) published (Venkateshwarlu and Bharti, 2022b) recently are included in this study, wherever required for comparison purposes only. Furthermore, our recent studies (Venkateshwarlu and Bharti, 2021, 2022b,a) have established the reliability and accuracy of the present modeling and simulation approaches via a thorough comparison of results with the earlier experimental and numerical studies in terms of droplet length, effective diameter, and radius of the interface evolution for broader flow operating conditions. The validation of results, thus, is not reported herein to avoid repetition. Based on our earlier experience (Venkateshwarlu and Bharti, 2021, 2022b,a), the subsequent presented results are believed to have excellent ( $\pm 1-2\%$ ) accuracy.

#### 4.1. Instantaneous phase flow and droplet formation profiles

Based on the instantaneous evolution of phases ( $\phi$ ) and liquid-liquid interface (LLI), a detailed discussion on the periodic time cycle and droplet pinch-off mechanism at a fixed contact angle ( $\theta = 135^\circ$ ) have been made in our recent study (Venkateshwarlu and Bharti, 2022b). In continuation, Figure 2 depicts a combined influence of contact angle ( $120^\circ \leq \theta \leq 180^\circ$ ) and flow rate ratio ( $0.1 \leq Q_r \leq 10$ ) on the periodic time cycle of the droplet formation, which is classified into five stages (S0 - initial, S1 - filling, S2 - squeezing, S3 - pinch-off, and S4 - stable droplet) under the squeezing ( $Ca_c < 10^{-2}$ ) flow regime.

First, both phases are injected simultaneously through respective channel inlets. The initial stage (S0) ends at time  $t_0 = 0$  when the vertical channel is completely filled with the dispersed phase (DP). Subsequently, DP starts intruding into the primary channel at the starting of the filling stage (S1) at time  $t_0$ . The dispersed phase evolves as a convex shape and expands until it reaches the opposite wall of the main channel at the end of S1 at time  $t_1$ . At  $Q_r = 1$ , the dispersed phase touches the top wall for both hydrophobic ( $120^\circ \leq \theta \leq 150^\circ$ ) and superhydrophobic ( $150^\circ < \theta \leq 180^\circ$ ) conditions. In this case, both CP and DP, having equal viscosity, are flowing with the same flow rate. Therefore, the wall effects have become more potent with increasing contact angle. The filling time is thus smoothly increasing with

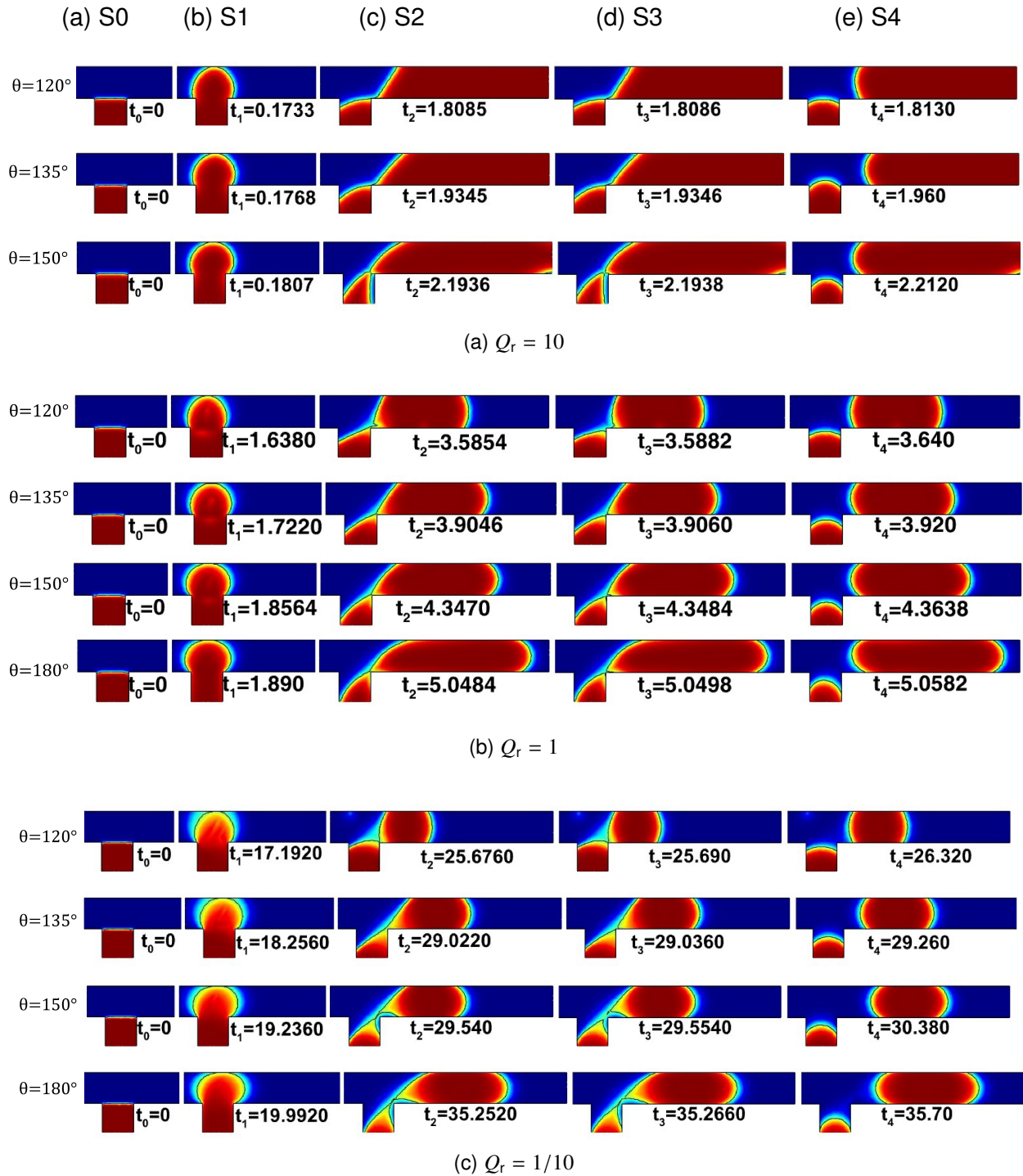


Figure 2: Instantaneous phase composition profiles and the droplet formation stages (S0 - initial, S1 - filling, S2 - squeezing, S3 - pinch-off, and S4 - stable droplet) as a function of flow rate ratio ( $Q_r$ ) and contact angle ( $\theta$ ) for a fixed capillary number ( $Ca_c = 10^{-4}$ ). The dimensionless time ( $t_0$  to  $t_4$ ) refers to end of each stage.

increasing contact angle. Similarly, there is a smooth increase in the filling time for extreme flow rate conditions,  $Q_r = 10$  and  $1/10$  under both the hydrophobic and superhydrophobic conditions. The filling or growing stage S1 ends at time  $t_1$  when the continuous phase flow is blocked by the dispersed phase due to the equilibrium between the forces arising from interfacial tension and squeezing pressure. However, a narrow gap exists between the wall and interface that allows the continuous phase to flow. Nonetheless, the gap between the interface and channel wall is reduced, leading to the hydrodynamic force exerted by the surrounding fluid on the droplet causes to deform (van Steijn et al., 2010).

The filling time ( $t_f = t_1 - t_0$ ) is correlated as a function of  $Q_r$ ,  $Ca_c$  and  $\theta$  ( $0.1 \leq Q_r \leq 10$ ,  $120^\circ \leq \theta \leq 180^\circ$ , and  $10^{-4} \leq Ca_c \leq 10^{-3}$ ) as follows:

$$t_f = ACa_c^B Q_r^C \quad (9)$$

where

$$A = \alpha + \beta\theta^{2.5} + \gamma\theta^3, \quad B = \alpha + \beta\theta^{2.5} + \gamma\theta^{-2}, \quad C = \alpha + \beta\theta^{2.5} + \gamma\theta^3$$

Statistical non-linear regression analysis is performed to obtain the correlation coefficients of  $t_f$  with DataFit (trial version) and MATLAB tools and their values are presented in Table 1.

The growing dispersed phase moves downstream as time progresses, and this stage is called squeezing (S2) as the surrounding fluid starts exerting viscous shear on the interface due to the pressure developed upstream of the main channel. The dispersed phase now has two sides: front and rear. The front side shape does not change with time and position; however, the interface curvature changes from convex to concave on the rear side. For a smaller contact angle, the interaction between the channel wall surface and droplet becomes stronger. Hence, the squeezing time ( $t_s = t_2 - t_1$ ) increases with the contact angle as the surface offers higher resistance.

The time required by the squeezing stage  $t_s = (t_2 - t_1)$  is best correlated as a function of  $Q_r$ ,

Table 1: Statistical correlation coefficients and parameters.

Relation		$\alpha$	$\beta$	$\gamma$	$\zeta$	$\delta_{\min}(\%)$	$\delta_{\max}(\%)$	$R^2$
Eq. (9)	A	1.3067	$1.7163 \times 10^{-5}$	$-1.2358 \times 10^{-6}$	-	0.0063	5.8633	0.9992
	B	0.0421	$-1.1329 \times 10^{-7}$	-131.5744	-			
	C	-1.0260	$4.9780 \times 10^{-7}$	$-4.2857 \times 10^{-8}$	-			
Eq. (10)	A	7.8576	-0.6008	-30.048	-	0.2204	6.6781	0.9929
	B	0.0019	0.0010	-0.0011	-			
	C	-0.0766	-0.0170	$6.5148 \times 10^{-5}$	-			
	D	5199.1216	9615.2693	1298.1974	-			
	E	0.0026	-0.1570	0.0056	-			
	F	$-7.8343 \times 10^5$	$1.2337 \times 10^4$	44.3553	-			
Eq. (11)	A	0.0037	$-1.6227 \times 10^{-4}$	$4.4983 \times 10^{-5}$	-	0.2397	8.1216	0.9940
	B	0.0317	$-3.1369 \times 10^{-3}$	$9.0569 \times 10^{-4}$	-			
	C	3.9705	-1.8292	0.2755	-0.0135			
	D	-230.58	101.08	-14.533	0.718			
	E	$3.6861 \times 10^{-5}$	-0.0022	$-2.7062 \times 10^{-6}$	-			
	F	26.015	-13.193	2.2006	-0.1219			
Eq. (12)	A	5597.2289	$-9.18 \times 10^{-3}$	$2.83 \times 10^{-5}$	-	0.0337	7.7721	0.9976
	B	$-2.8920 \times 10^5$	$-5.8981 \times 10^3$	$1.9482 \times 10^{-3}$	-			
	C	1340.7634	$-2.90 \times 10^{-2}$	$2.0 \times 10^{-3}$	-			
	D	-1840.9596	1572.3580	-20476.5479	-			
	E	-1409.3022	$9.2296 \times 10^6$	$-8.0480 \times 10^7$	-			
Eq. (13)	A	-0.3352	20.4687	-104.5415	-	0.0846	6.0235	0.9955
	B	-2926.2562	-145.4043	943.3530	-			
	C	-2.0346	0.3018	2.0033	-			
	D	6.2976	-0.5135	-27.9788	-			
	E	-2.5380	13.9446	-5390.5463	-			
	F	$6.5432 \times 10^{-5}$	0.3142	-0.7944	-			
Eq. (14)	A	1.3166	-19.3372	10786.2346	-	0.0031	4.9505	0.9516
	B	-134.1631	-7.8858	69.9675	-			
	C	-183.6308	-46.2430	135.6212	-			
	D	0.1515	-3.8498	2.5792	-			
	E	-0.1871	$-1.8985 \times 10^{-4}$	0.0273	-			
	F	$-1.5830 \times 10^{-5}$	-0.0136	$4.9666 \times 10^{-5}$	-			

$Ca_c$  and  $\theta$  ( $0.125 \leq Q_r \leq 10$ ,  $120^\circ \leq \theta \leq 180^\circ$ , and  $10^{-4} \leq Ca_c \leq 10^{-3}$ ) as follows.

$$t_s = X_s t_f \quad (10)$$

where

$$\begin{aligned}
 X_s &= A + B/Ca_c + CQ_r + DQ_r^2 + EQ_r^3 + FQ_r^4, \\
 A &= \alpha + \beta m / \log(m) + \gamma m^{-2} \log(m), & B &= \alpha + \beta m^{2.5} + \gamma e^m, & C &= \alpha / (1 + \beta \theta + \gamma \theta^2), \\
 D &= \alpha + \beta m \log(m) + \gamma \log(m), & E &= \alpha / (1 + \beta q + \gamma q^2), & F &= \theta / (\alpha + \beta \theta - \gamma \theta^2) \\
 m &= 10^{-3} \theta, & q &= 10^{-1} \theta
 \end{aligned}$$

Statistical non-linear regression analysis is performed to obtain the correlation coefficients of  $X_s$  with DataFit (trial version) and MATLAB tools and their values are presented in Table 1.

On moving further, the interface on the rear side of the dispersed phase collapses as time progresses and forms a droplet. Hence, this stage is called pinch-off (S3). The degree of confinement of the droplets reduces when the shear forces dominate the breakup process (Glawdel et al., 2012; Bashir et al., 2014). For larger  $\theta$ , the degree of confinement promotes the breakup, whereas for smaller  $\theta$ , the degree of confinement suppresses the breakup. The wall provides less resistance to the droplet in the superhydrophobic regime and accelerates the droplet formation. It can be observed that the droplet shape is also changing when the surface wettability is different. Therefore, each stage of the droplet formation is directly influenced by the contact angle.

The time required by the spontaneous pinch-off (S3) stage is  $t_b = (t_3 - t_2) \lll 1$ , and best correlated as a function  $Q_r$ ,  $Ca_c$  and  $\theta$  ( $0.125 \leq Q_r \leq 10$ ,  $120^\circ \leq \theta \leq 180^\circ$ , and  $10^{-4} \leq Ca_c \leq 10^{-3}$ ) as follows:

$$t_b = X_b t_s \quad (11)$$

where,

$$\begin{aligned}
 X_b &= A + B/x_1 + C/Q_r + D/x_1^2 + E/Q_r^2 + F/(x_1 Q_r), \\
 A &= \alpha + \beta/m^{1.5} + \gamma/m^2, & B &= \alpha + \beta/m^{1.5} + \gamma/m^2, & C &= \alpha m^3 + \beta m^2 + \gamma m + \zeta, \\
 D &= \alpha m^3 + \beta m^2 + \gamma m + \zeta, & E &= \alpha + \beta s^3 + \gamma/s^{1.5}, & F &= \alpha m^3 + \beta m^2 + \gamma m + \zeta, \\
 x_1 &= \log Ca_c, & m &= 10^{-3}\theta, & s &= \log \theta
 \end{aligned}$$

Statistical non-linear regression analysis is performed to obtain the correlation coefficients of  $X_b$  with DataFit (trial version) and MATLAB tools and their values are presented in Table 1.

After the pinch-off, the droplet attains a stable shape and does not change anymore when it is allowed to move downstream further as the development of the droplet size is completely achieved, and this stage is called the stable droplet (S4). The stable droplet time is defined as,  $t_{sd} = t_4 - t_3$ .

It is, therefore, concluded that the total time needed for one complete cycle (S0 to S3) of the droplet breakup or pinch-off as  $t_p = (t_f + t_s + t_b)$  and that of the stable droplet,  $t_d = (t_p + t_{sd})$ . The flow of CP and DP continues during the process of droplet formation. However, the time needed for each droplet formation stage depends upon the capillary number ( $Ca_c$ ) and flow rate ratio ( $Q_r$ ), and contact angle ( $\theta$ ). Further insights of droplet formation and its dynamics are provided in the following section in terms of the evolution of interface.

Overall, the flow map presents the droplet formation stages as a function of the contact angle and capillary number; both the filling ( $t_1$ ) and pinch-off ( $t_3$ ) time decrease with an increase in the flow rate ratio for a given contact angle, as shown in Figures 3a and 3b. It can be observed that the contact angle effect is marginal in the filling stage because of the less dominance of surface forces; however, the contact angle effect is dominant in the pinch-off stage as the interaction between the three phases: CP, DP, and the wall, is substantial. Further, a gradient ( $X_i = \Delta t_i / \Delta Q_r$ ) has been plotted against the flow rate ratio ( $Q_r$ ) in Figures 3c and 3d to elaborate the influence of  $Q_r$  and  $\theta$  on  $t_1$  and  $t_3$ . The  $X_i$  has shown inverse dependence on  $Q_r$  and proportional dependence on  $\theta$ . Both  $X_1$  and  $X_3$  decrease non-linearly (i.e., exponential or



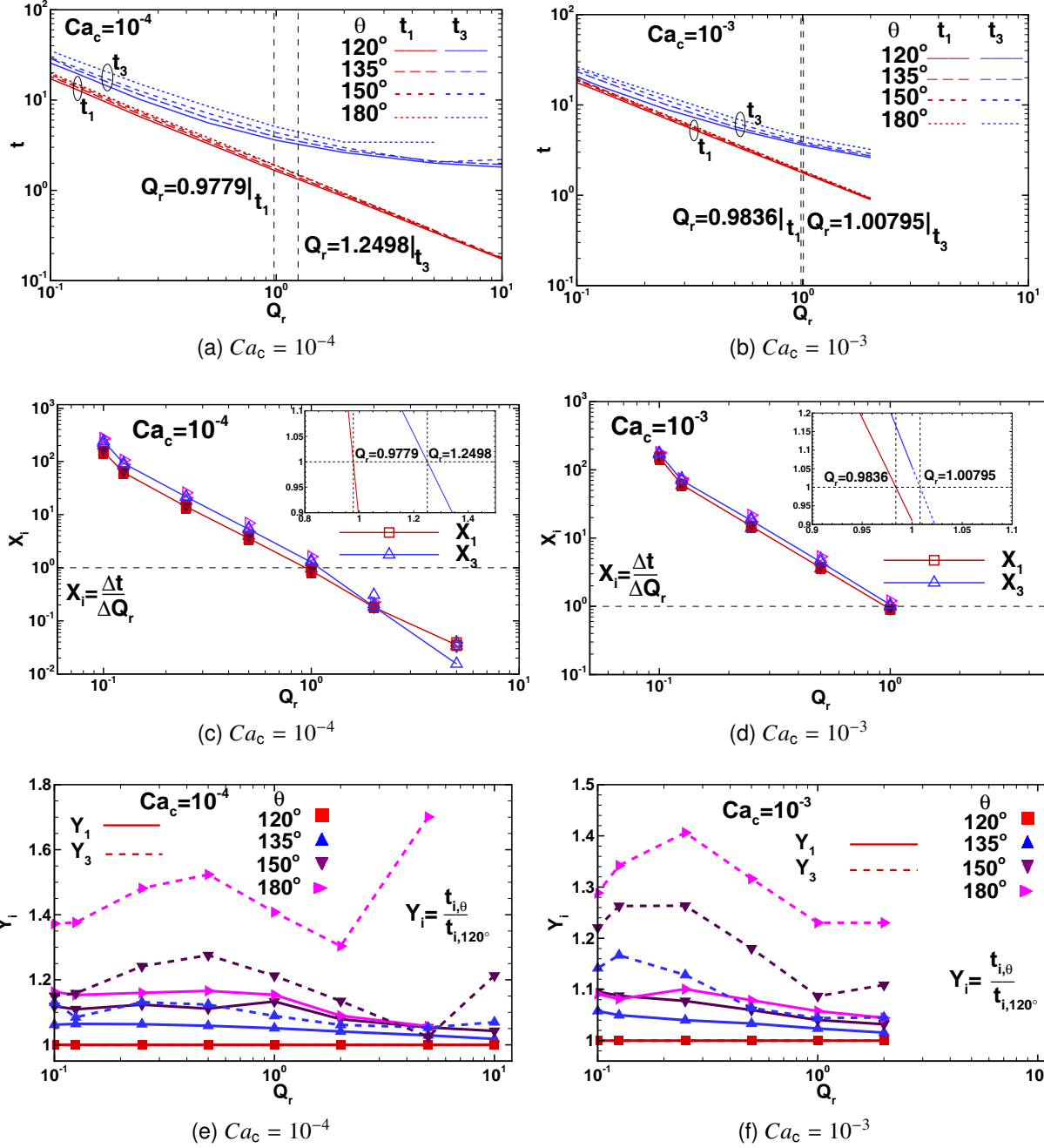


Figure 3: Flow map, time ratio ( $Y_i$ ), gradient ( $X_i$ ) of filling and pinch-off stages of the droplet as a function of contact angle ( $\theta$ ) and flow rate ratio ( $Q_r$ ).

power-law) up to a threshold value of  $Q_r = 0.9779$  and  $Q_r = 1.2498$  for  $Ca_c = 10^{-4}$ , and similarly,  $Q_r = 0.9836$  and  $Q_r = 1.00795$  for  $Ca_c = 10^{-3}$  (refer dashed line in Figures 3a to 3d) where the gradient becomes unity ( $X_i = 1$ ) for all values of contact angle. Beyond these critical values of  $Q_r$ , the filling time is slightly influenced by the contact angle. However, the pinch-off time is strongly influenced by the superhydrophobic ( $\theta \geq 150^\circ$ ) nature of the surface.

Furthermore, time ratio ( $Y_i = t_{i,\theta}/t_{i,120^\circ}$ ) parameter is introduced and plotted in Figures 3e and 3f to elucidate the effect of the contact angle on filling ( $t_1$ ) and pinch-off ( $t_3$ ) time. It can clearly be observed that both filling and pinch-off time strongly depend on the contact angle, as reflected by  $Y_i > 1$ , in contrast to non-noticeable effects seen in Figures 3a to 3d. A difference of about 5-10 % between the estimates of  $t_1$  and  $t_3$  can be noticed vividly. It may thus be concluded that both flow rate ratio and contact angle strongly influence the droplet formation cycle. The evolution of interface is further explored in the subsequent section.

## 4.2. Evolution of the instantaneous interface

The evolution of the interface ( $x$  vs  $y$  at  $\phi = 0.5$ ) profile in the filling and squeezing stages with the time are depicted for  $Q_r = 1$  at  $Ca_c = 10^{-4}$  in Figure 4. The numerical data of curvature of the interface has been extracted and plotted as a function of time and contact angle. Depending upon the contact angle, the interface attains a specific shape and shows distinct variation accordingly. In the first stage (filling), the droplet is expanding without showing much movement towards the downstream direction. It can be observed that at  $\theta = 120^\circ$ , the filling time is equal to 1.638 (refer to Figure 4a), and for  $\theta = 180^\circ$ , it has increased to 1.890 (refer to Figure 4e). The interface is evolving slowly at  $120^\circ$  and becoming smooth with an increase in the contact angle. The continuous phase is wetting channel walls more than the dispersed phase. The surface energy of the solid walls in contact with the fluid decreases with an increase in the contact angle from  $120^\circ$  to  $180^\circ$ . Because the dispersed phase entering the horizontal channel would take up more fluid in the droplet formation owing to the force due to the contact angle that further leads to attachment to the bottom surface rather than to the

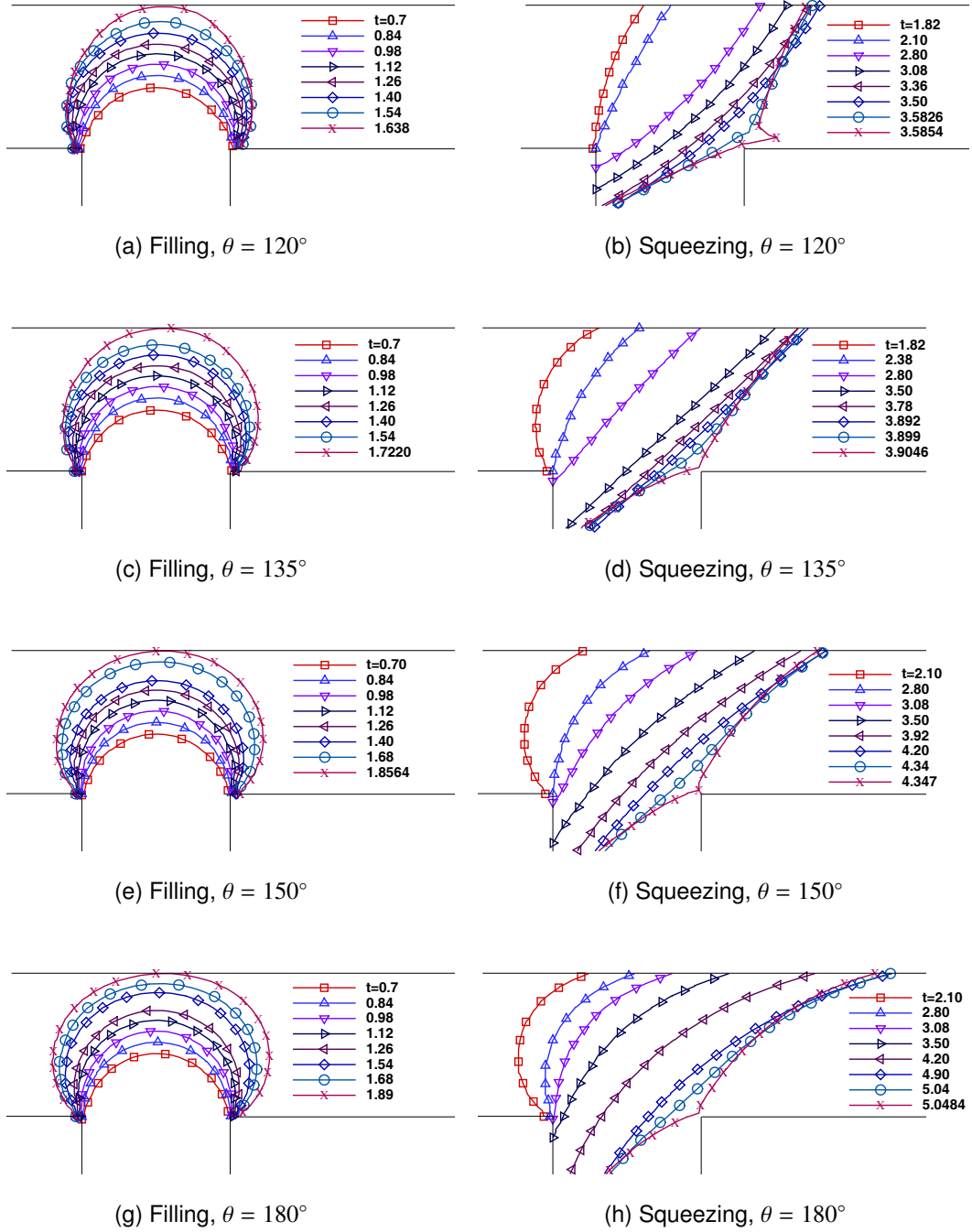


Figure 4: Evolution of the interface during the filling and squeezing stage as a function contact angle ( $\theta$ ) for  $Ca_c = 10^{-4}$  at  $Q_r = 1$

top surface. Hence, the filling time is increasing from  $120^\circ - 180^\circ$  due to the high resistance encountered by the dispersed phase from the solid surface and changing the evolution of the interface. Thus, the total time for the interface to touch the opposite wall of the channel is also

increasing.

Further, the dispersed phase starts moving downstream in the squeezing stage as the surrounding fluid pushes it, as shown in Figures 4b, d, f and h. The evolution of the rear side of the interface is plotted as a function of time. At lower contact angles,  $\theta = 120^\circ$ , the interface is seen in a convex shape early, which quickly transforms into concave (refer to Figure 4b). The interface attaining a concave shape lately at higher contact angles,  $\theta = 135^\circ - 180^\circ$  (refer to Figure 4d, f and h). Therefore, it can be concluded that the interactive force between the channel wall and dispersed phase is getting reduced. The interface shape with larger curvature is attributed mainly due to the dominance of the capillary forces at the higher contact angles ( $\theta = 135^\circ - 180^\circ$ ).

The dispersed phase enters into the primary channel until the interface collapses and forms a droplet, as shown in Figure 5. In the filling stage, DP forces are dominant over CP. Hence, the droplet is expanding without showing much movement towards the downstream direction. It can be observed that the filling time is equal to 0.1733 at  $\theta = 120^\circ$ , which has increased to 0.1807 at  $\theta = 150^\circ$  for  $Q_r = 10$  (refer to Figure 5a). Hence, the filling time is increasing from  $120^\circ - 150^\circ$  due to the high resistance from the wall. The continuous phase will flow through the small gap between the wall and interface in the squeezing stage (van Steijn et al., 2010). The interaction between the solid wall and droplet is more vital in the case of  $\theta = 120^\circ$  and becoming weaker at  $\theta = 150^\circ$  as shown in Figure 5b. Notably, the interface shape is stretching and trying to attain a circular shape for superhydrophobic conditions. Hence, the time of the squeezing stage is increasing from  $t = 1.8085$  to 2.1936 (refer to Figure 5b). After that, the interface becomes unstable and collapses from the mainstream. Moreover, the pinch-off point moves away from the T-junction towards the downstream when  $\theta = 120^\circ$  and breakup is happening exactly at the junction point for  $135^\circ \leq \theta \leq 180^\circ$ . Therefore, it can be concluded that the breakup location is the point where the forces responsible for the pinch-off are balanced. The filling time for  $120^\circ - 180^\circ$  is increasing from  $t = 1.638$  to 1.890 for  $Q_r = 1$  (refer to Figure 5c). This is happening due to less contact of the dispersed phase with the solid. In the

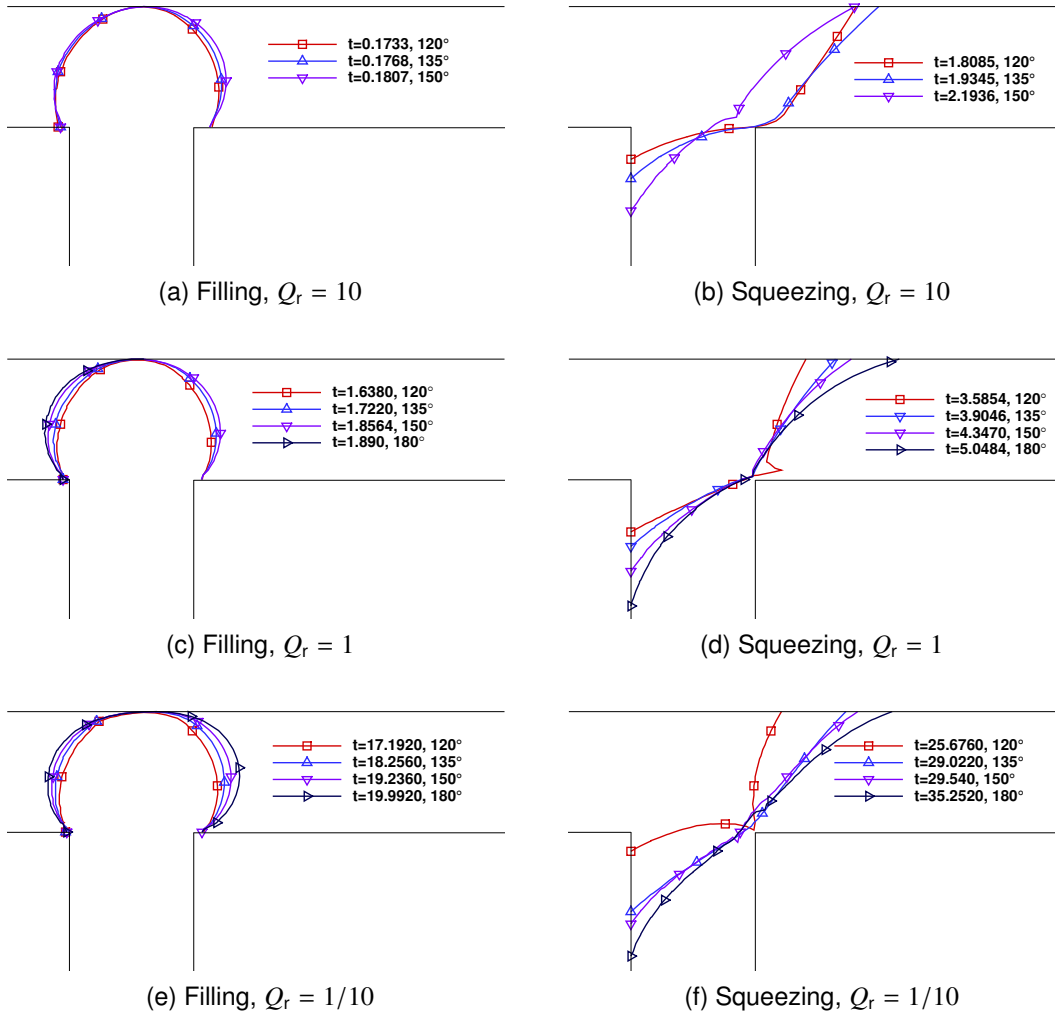


Figure 5: Evolution of the interface during the filling and squeezing stages as a function of flow rate ratio ( $Q_r$ ) and contact angle ( $\theta$ ) for  $Ca_c = 10^{-4}$

squeezing stage, the continuous phase flows around the dispersed phase until it pinches-off. The larger curvature obtains the interface shape due to the dominance of the capillary forces. The interface exhibited a convex shape for superhydrophobic surfaces; however, more planar-like behavior is observed for the hydrophobic surfaces. At the pinch-off point, the interface is seen as a sharp bending for  $120^\circ \leq \theta \leq 150^\circ$  and a smooth for  $\theta > 150^\circ$ . At  $\theta = 180^\circ$ , the interface is evolving smoothly in the squeezing stage. Moreover, at the same time, the interaction between the wall and the interface is becoming weaker. Hence, the filling and squeezing timings are decreasing. At lower  $Q_r = 1/10$ , the interface expands horizontally for

the filling stage. The nose of the droplet is touching the opposite wall and moves towards the downstream by increasing the contact angle ( $\theta$ ) from  $120^\circ - 180^\circ$ , as shown in Figure 5e. Hence, the filling time is also increasing. The interface curvature is changing into a concave shape faster for  $120^\circ \leq \theta \leq 135^\circ$ . However, the interface is sustaining to be in convex until the pinch-off time for  $\theta \geq 150^\circ$ . It is interesting to see that the pinch-off point at the right corner of T-junction point for all values of the contact angles. The following section presents the effect of contact angle on the interface evolution in terms of the instantaneous evolution of the pressure in the continuous and dispersed phases.

### 4.3. Pressure evolution

The surface wettability effects are more significant in the evolutions of pressure in the continuous ( $p_{cp}$ ) and dispersed phases ( $p_{dp}$ ). The pressure evolutions have been measured during the droplet formation by choosing two different locations, one in the continuous phase ( $p_{cp}$ ) and the second in the dispersed phase ( $p_{dp}$ ), as shown in Figure 1a. During the early stage of the droplet formation, the dispersed phase invades into the main channel and slowly restricts the flow of the continuous phase. Once the filling stage is completed, the continuous phase flow is obstructed leads to a rise in the upstream pressure ( $p_{cp}$ ). The process continues until  $p_{cp}$  reaches a maximum value and then a sudden fall at the pinch-off point wherein the droplet breaks off from the dispersed phase. Earlier studies reported that pressure ( $p_{dp}$ ) in the dispersed phase is constant (Garstecki et al., 2006; Bashir et al., 2014). However, we observed that  $p_{dp}$  is not constant during the filling stage, but it oscillates in an anti-phase with  $p_{cp}$  (Abate et al., 2012). After crossing the filling stage,  $p_{dp}$  is showing gradual increase up to the pinch-off point. It is noticed that at the pinch-off, both  $p_{dp}$  and  $p_{cp}$  are showing a sudden falling trend, as shown in Figure 6.

At higher values of  $Q_r (= 10)$ ,  $p_{cp}$  and  $p_{dp}$  are not showing much variation with the contact angle ( $\theta$ ) during the filling stage and it can be observed in Figure 6a-b. However, in the squeezing stage,  $p_{cp}$  and  $p_{dp}$  increase with increase in  $\theta$ . This is attributed mainly due to the confinement

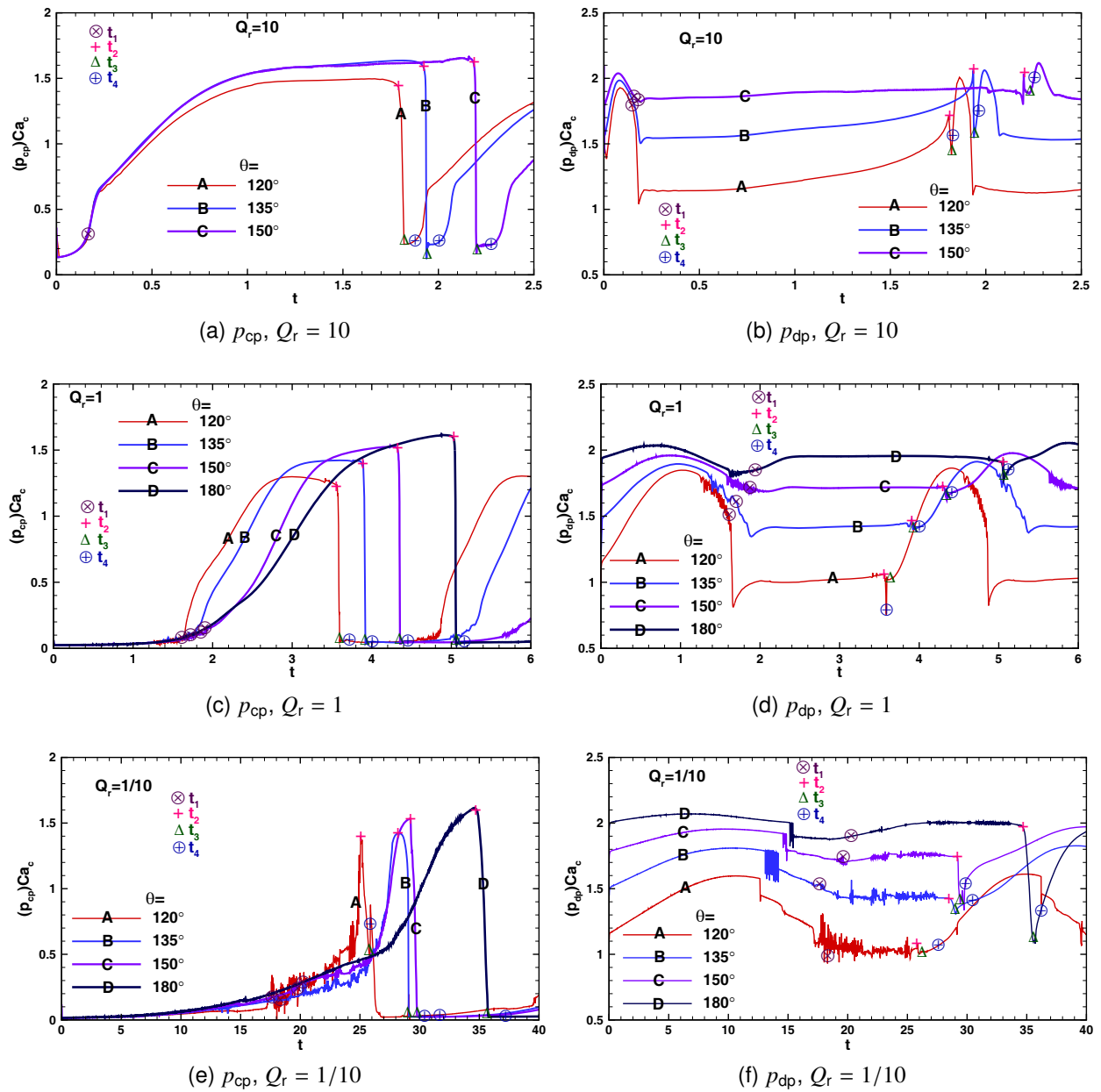


Figure 6: Evolution of the pressure in the continuous ( $p_{cp}$ ) and dispersed ( $p_{dp}$ ) phases as a function the flow rate ratio ( $Q_r$ ), and contact angle ( $\theta$ ) for  $Ca_c = 10^{-4}$ . The filling, squeezing, pinch-off and stable droplet time are marked with  $\otimes$ ,  $+$ ,  $\Delta$ , and  $\oplus$ , respectively.

of the flow. The variations in  $p_{dp}$  with respect to  $\theta$  are increasing at  $Q_r = 1$  and 10.

Maximum pressure in CP ( $p_{cp,max}$ ) as a function of  $Q_r$ ,  $Ca_c$  and  $\theta$  ( $0.1 \leq Q_r \leq 10$ ,  $120^\circ \leq \theta \leq$

180°, and  $10^{-4} \leq Ca_c \leq 10^{-3}$ ) is given by the following correlation:

$$p_{cp,max} = A + BCa_c^{0.5} + Cx_2 + Dx_2^2 + Ex_2^3 \quad (12)$$

where

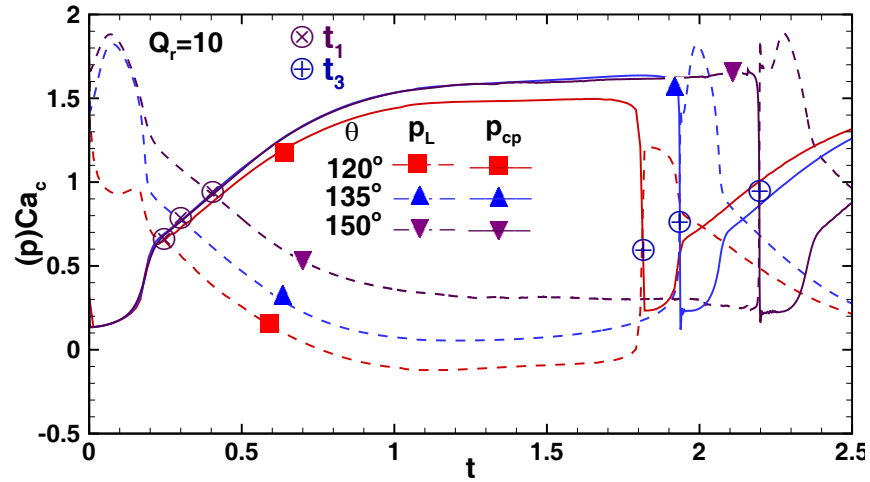
$$\begin{aligned} x_2 = \log Q_r, \quad A = \alpha/(1 + \beta\theta + \gamma\theta^2), \quad B = \alpha + \beta q^{1.5} + \gamma e^q, \quad C = \alpha + \beta\theta^{2.5} + \gamma\theta^3, \\ D = \alpha + \beta w^3 + \gamma(\log w)^2, \quad E = \alpha + \beta/\theta^{1.5} + \gamma/\theta^2, \quad q = 10^{-1}\theta, \quad w = 10^{-2}\theta, \end{aligned}$$

Statistical non-linear regression analysis is performed to obtain the correlation coefficients for  $p_{cp,max}$  with DataFit (trial version) and MATLAB tools and their values are presented in Table 1. The Laplace pressure plays a vital role in the interface shape evolution and it is essentially the difference between  $p_{dp}$  and  $p_{cp}$ . For instance, if  $p_L$  is small, the radius of the curvature of the interface is large leads to adopting a flattened shape. Nevertheless, the interface adopts a more curved shape with a smaller radius of curvature when  $p_L$  is large. The effect of the contact angle ( $\theta$ ) on the Laplace pressure ( $p_L$ ) is seen in Figure 7. At higher flow rate ratios ( $Q_r = 10$ ),  $p_L$  is increasing in the starting period then slowly decreases (refer to Figures 7a-c). Therefore, it indicates that the interface is transiting from a more curved into flattened shape. When  $Q_r = 10$ ,  $p_L$  is continuously decreasing for  $\theta = 120^\circ$ . Whereas there is a rise and then decrease for  $\theta = 135^\circ$  and  $150^\circ$ . At  $Q_r = 1$  and  $1/10$ ,  $p_L$  is not shown much variation for superhydrophobic conditions ( $\theta > 150^\circ$ ), but there is an increase in  $p_L$  in the initial period for  $\theta = 120^\circ$  and  $135^\circ$ , as shown in Figures 7a-c.

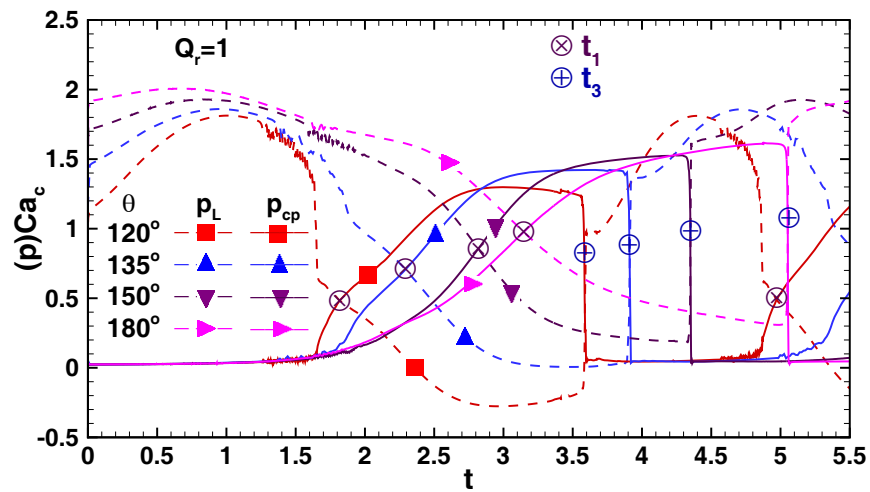
It can also be observed from the point where both  $p_{cp}$  and  $p_L$  are intersecting indicates the end of the filling stage, marked with symbol  $\otimes$ ,  $t_1$ .  $t_1$  is increasing as  $\theta$  increases. For instance,  $t_1 = 0.196$  for  $\theta = 120^\circ$  and  $0.404$  for  $\theta = 150^\circ$  when  $Q_r = 10$  (refer to Figure 7a).

Further, the pinch-off time ( $t_3$ ) can be predicted from the point where  $p_{cp}$  and  $p_L$  are intersecting for the second time, marked with symbol  $\oplus$ ,  $t_3$ . It is increasing with increasing contact angle, as shown in Figure 7. For instance,  $t_3 = 1.810$  for  $\theta = 120^\circ$  and  $2.196$  for  $\theta = 150^\circ$  when  $Q_r = 10$  (refer to Figure 7a). A correlation is proposed to predict the pinch-off time ( $t_3$ ) based

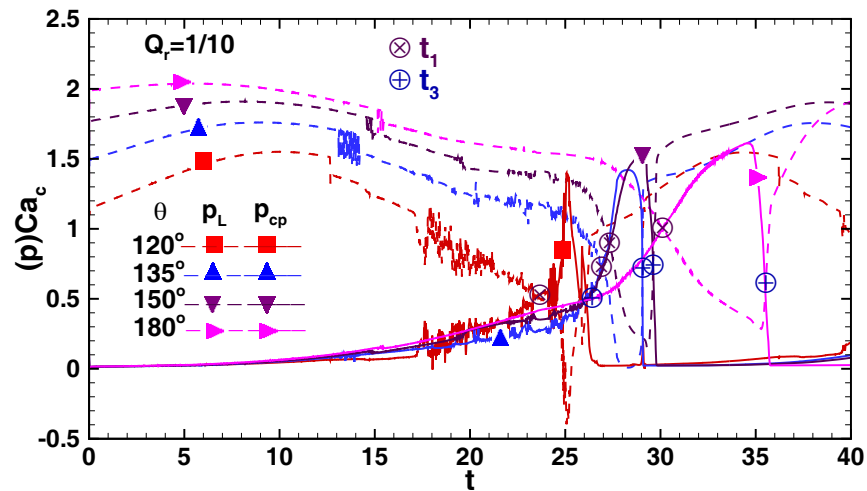




(a)  $Q_r = 10$



(b)  $Q_r = 1$



(c)  $Q_r = 1/10$

Figure 7: Evolution of the instantaneous pressure for as a function of the flow rate ratio ( $Q_r$ ) and contact angle ( $\theta$ ) for  $Ca_c = 10^{-4}$ . The filling and pinch-off time are marked with  $\otimes$  and  $\oplus$ , respectively.

on the pressure evolution profiles as a function of contact angle (refer to Figure 7) as follows:

$$t_{3,p} = A + BCa_c^{0.5} + C/Q_r + D/Q_r^2 + E/Q_r^3 + F/Q_r^4 \quad (13)$$

where

$$\begin{aligned} A &= \alpha + \beta w^2 \log w + \gamma s^2, & B &= \alpha + \beta \theta^{0.5} + \gamma s, & C &= \alpha + \beta e^p + \gamma/p^2, \\ D &= \alpha + \beta/\log z + \gamma(\log z)/z^2, & E &= \alpha + \beta/s + \gamma/\theta^2, & F &= \alpha/(1 + \beta p + \gamma p^2), \\ w &= 10^{-2}\theta, & s &= \log \theta, & p &= \sec \theta, & z &= \cot \theta \end{aligned}$$

Statistical non-linear regression analysis is performed to obtain the correlation coefficients for  $t_{3,p}$  with DataFit (trial version) and MATLAB tools and their values are presented in Table 1.

Figure 8 shows the comparison of the filling ( $t_1$ , filled symbols) and pinch-off ( $t_3$ , unfilled symbols) time based on the phase and pressure profiles. The pressure in the continuous phase starts to rise after the dispersed phase reaches the opposite wall. Hence, the filling time ( $t_1$ ) predicted based on the pressure profile, is higher than the phase profile. Thus, the

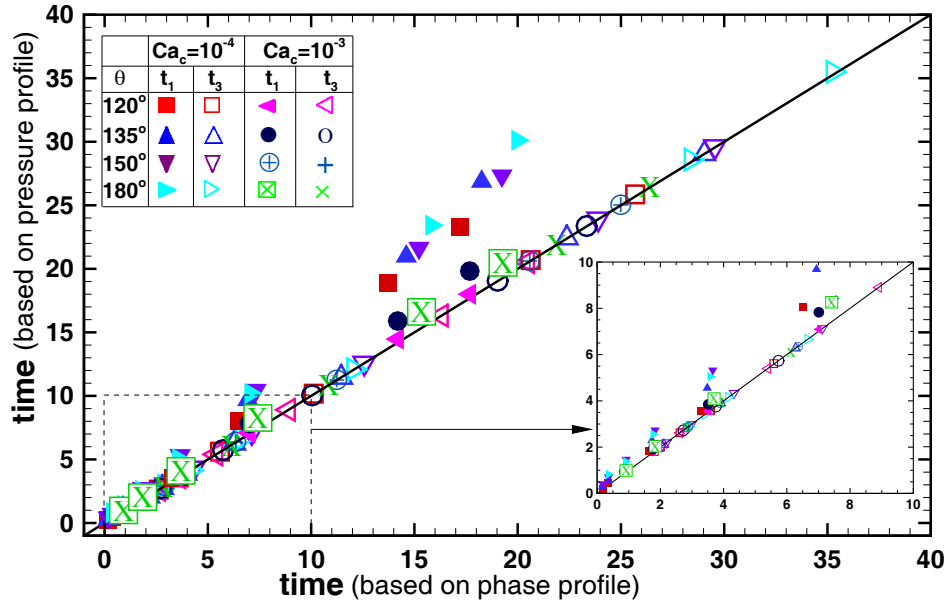


Figure 8: Comparison of the filling ( $t_1$ ) and pinch-off times ( $t_3$ ) obtained from the phase and pressure profiles as a function of the contact angle and  $Q_r$ .

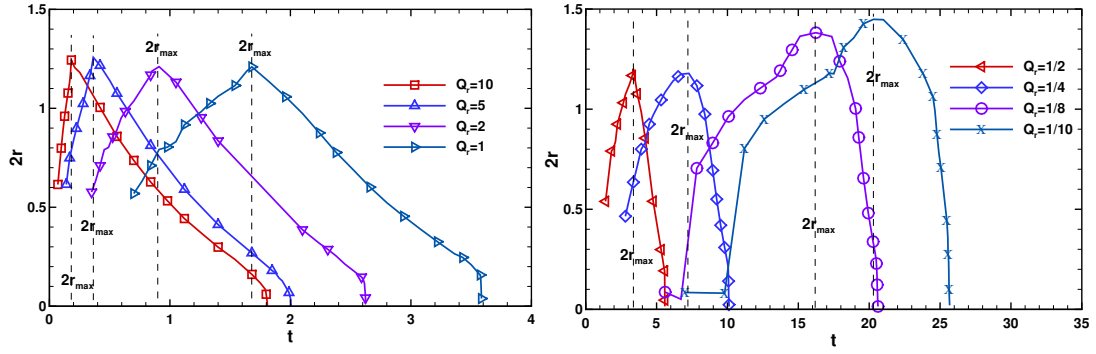
filling time ( $t_1$ ) points show more deviation. However, the pinch-off time ( $t_3$ ) matches the phase and pressure profiles for all the contact angles. In culmination, the droplet pinch-off mechanism can also be elucidated in depth by installing pressure sensors even without the flow visualization and image processing of the phase profiles.

#### 4.4. The droplet pinch-off mechanism

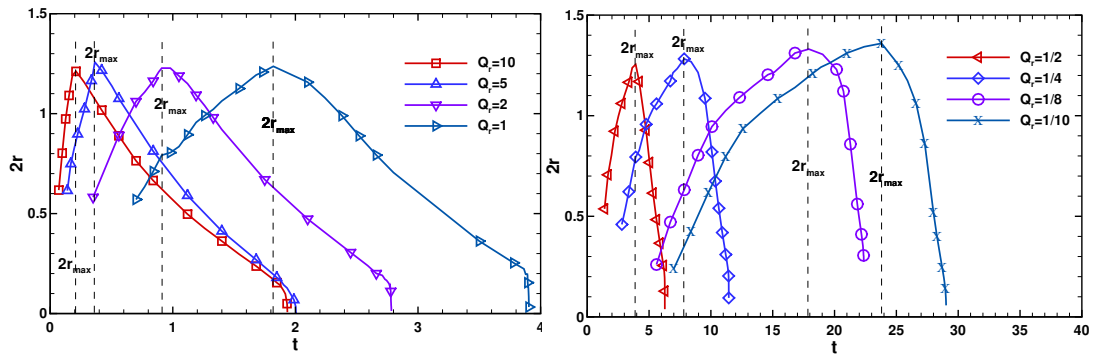
In this section, the droplet pinch-off mechanism is elucidated by analyzing the evolution of the interface and the Laplace pressure as a function of contact angle. In the filling stage, the dispersed phase starts penetrating the primary channel. The interface expands and progresses towards the opposite wall. The interface deforms as it experiences the hydrodynamic forces and attaining shape with a larger radius at the rear side and smaller at the front side. The corresponding Laplace pressure is sharply decreasing with time. Hence, the interface adopts a curvy shape with a smaller radius of curvature in the initial time and slowly transits into a flattened shape as time progresses.

Figure 9 describes the neck thickness ( $2r$ ) as a function of the flow rate ratio ( $Q_r$ ). For hydrophobic conditions ( $120^\circ \leq \theta < 150^\circ$ ),  $2r$  increases in the filling stage until it reaches a threshold value ( $2r_{\max}$ , marked with dashed lines) for lower  $Q_r$  values range from 1/2 to 1/10 (refer to Figure 9a,b). While  $2r_{\max}$  is increasing with decreasing  $Q_r$  ( $1/2 \geq Q_r \geq 1/10$ ), it is achieving the same value for higher  $Q_r$  ( $10 \leq Q_r \leq 1$ ). However, the neck thickness ( $2r$ ) has shown contrasting nature (refer to Figure 9c,d) for superhydrophobic conditions ( $150^\circ < \theta \leq 180^\circ$ ). Further, it can also be observed that the trend of the droplet pinch-off follows the same for both hydrophobic and superhydrophobic conditions. A correlation is developed to predict the value of  $2r_{\max}$  as a function of the contact angle as follows:

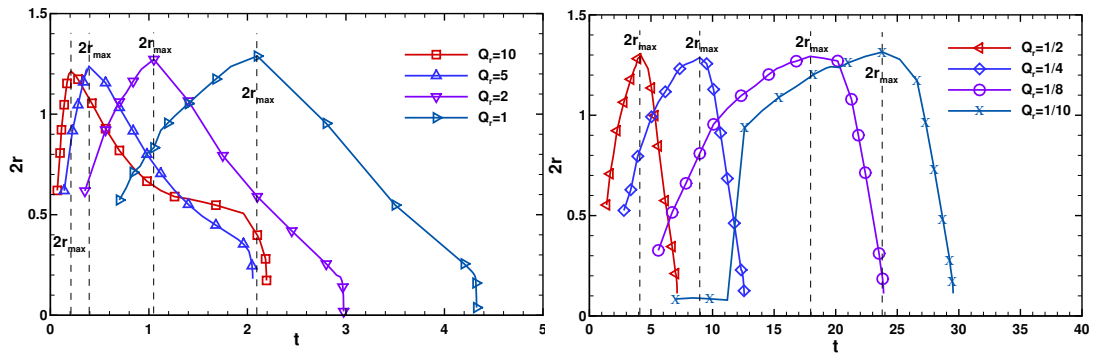
$$2r_{\max} = A + BCa_c + C/Q_r + D/Q_r^2 + E/Q_r^3 + F/Q_r^4 \quad (14)$$



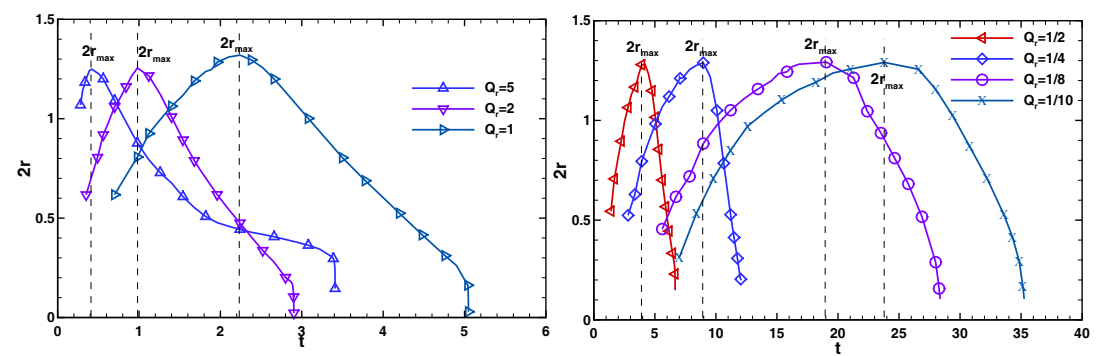
(a)  $\theta = 120^\circ$



(b)  $\theta = 135^\circ$



(c)  $\theta = 150^\circ$



(d)  $\theta = 180^\circ$

Figure 9: The interface neck thickness as a function of dimensionless time and contact angle ( $\theta$ ) at  $Ca_c = 10^{-4}$ .

where

$$\begin{aligned}
 A &= \alpha + \beta/q^2 + \gamma e^{-q}, & B &= \alpha + \beta \cos \theta + \gamma \sin \theta, & C &= \alpha + \beta(\log m)^2 + \gamma/m^{0.5}, \\
 D &= \alpha + \beta\theta^{2.5} + \gamma\theta^3, & E &= \alpha + \beta\theta \log \theta + \gamma\theta^{0.5}, & F &= \alpha/(1 + \beta\theta + \gamma\theta^2), \\
 q &= 10^{-1}\theta, & m &= 10^{-3}\theta
 \end{aligned}$$

Statistical non-linear regression analysis is performed to obtain the correlation coefficients with DataFit (trial version) and MATLAB tools and their values are presented in Table 1.

At the initial filling stage,  $2r$  increases smoothly up to a threshold value (marked with dashed lines). After that, the growth rate of radius at the backside decreases, as shown in Figure 10. The filling stage (dashed lines) is the point where both interfacial and shear forces are balanced. It is known that in the squeezing regime, the flow is essentially the pressure-driven. In the squeezing stage, the radius at the backside decreases with time smoothly. The droplet moves toward the downstream direction as its length increases further. At the pinch-off point, the radius approaches the minimum value, where the forces are balanced on the droplet, which is marked with dashed lines, as shown in Figure 10(I). When  $Q_r = 10$ ,  $2r$  increases at the early filling stage for the contact angle ( $\theta$ ) ranging from  $120^\circ \leq \theta \leq 150^\circ$ . Nevertheless, in the squeezing stage, the radius at the backside is comparatively high, and the droplet is expanding for  $\theta = 150^\circ$ , as shown in Figure 10a(I). The corresponding Laplace pressure ( $p_L$ ) across the interface is shown Figure 10a(II). The Laplace pressure ( $p_L$ ) is dropping smoothly in the filling stage for all the values of  $\theta$ . On moving further,  $p_L$  in the squeezing or necking decreases sharply for  $\theta = 120^\circ$  and smoothly for  $150^\circ$ . It can be observed that there is a sudden shoot-up in the  $p_L$  at the pinch-off point. Nonetheless, the pinch-off is taking place early in the case of  $\theta = 120^\circ$  and extending for  $150^\circ$ .

When  $Q_r = 1$ ,  $2r$  increases smoothly up to the threshold value in the early filling stage for all the values of  $\theta$ . Subsequently,  $2r$  decreases smoothly in the squeezing stage until the pinch-off point is marked with dashed lines, as shown in Figure 10b(I). However, there is a noticeable change in  $p_L$  acting on the interface for  $\theta = 120^\circ$ .  $p_L$  suddenly falls at the end of the filling

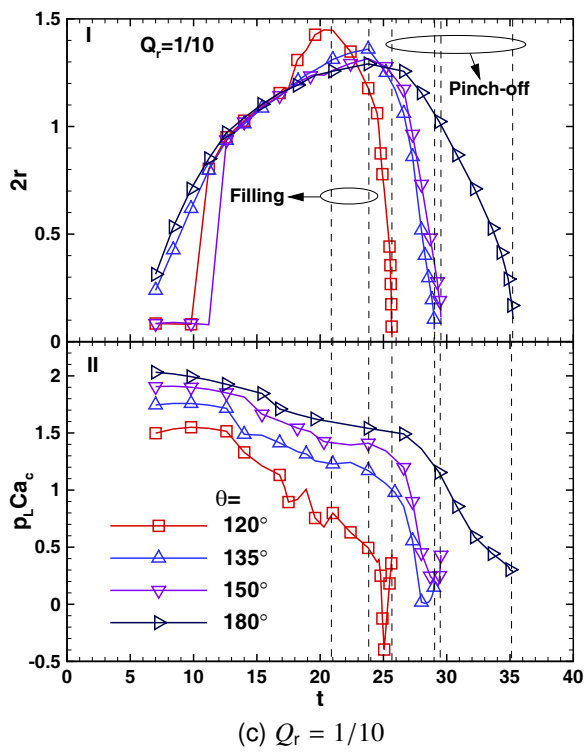
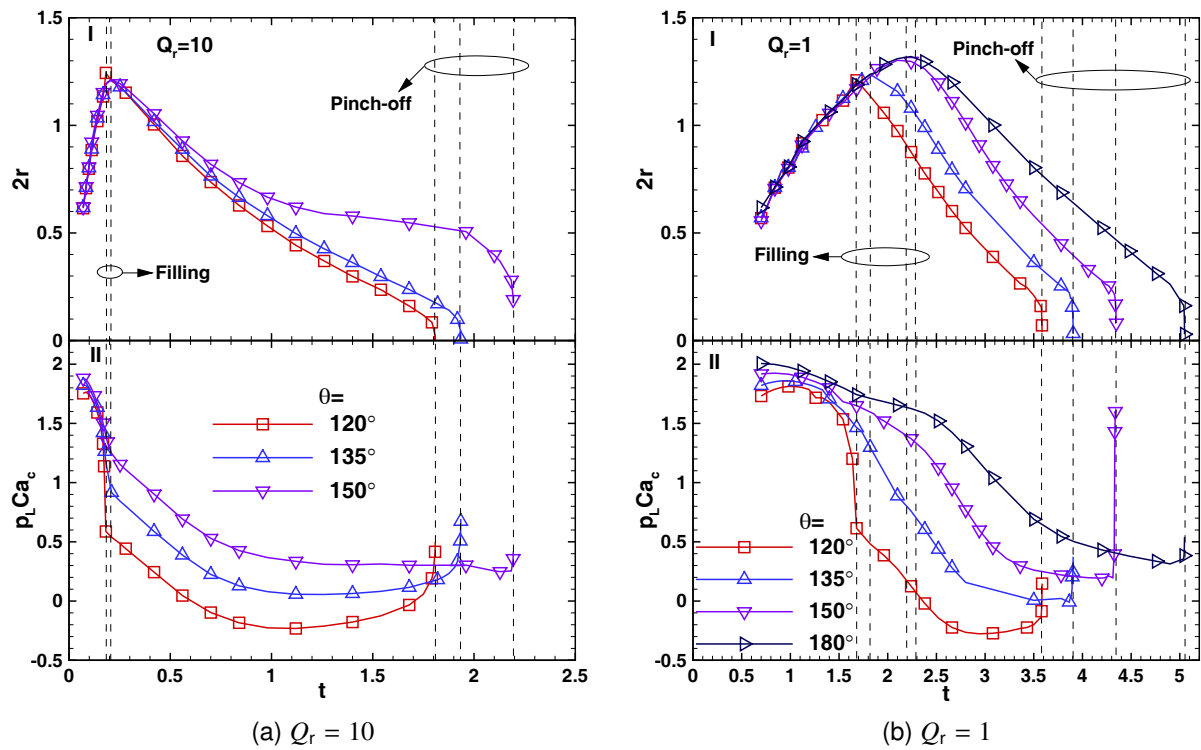


Figure 10: The droplet dynamics for  $Ca_c = 10^{-4}$  at  $\theta = 120^\circ - 180^\circ$  (a)  $Q_r = 10$ , (b)  $Q_r = 1$ , and (c)  $Q_r = 1/10$ .

stage, and subsequently, it decreases smoothly, as shown in Figure 10b(II). At the pinch-off point, there is a sudden shoot-up in  $p_L$ .

When  $Q_r = 1/10$ ,  $2r$  follows a sharp increase in the early filling stage. It can also be observed that for  $\theta = 120^\circ$ ,  $2r$  is shown smooth increasing variation in the filling stage and then sudden shoot-up and again drop. However,  $2r$  shows a smooth variation for  $\theta \geq 135^\circ$ , as shown in Figure 10c(I). The corresponding  $p_L$  is shown in Figure 10c(II). When  $\theta = 120^\circ$ ,  $\Delta p$  shows an oscillatory behavior in the filling stage. On moving further,  $p_L$  is falling suddenly in the squeezing and then again showing a shoot-up at the pinch-off point. The Laplace pressure for  $\theta \geq 135^\circ$  shows a smooth decrease and sudden rise at the pinch-off point. Therefore, it can be concluded that the solid surface is hydrophobic in nature, i.e.,  $\theta = 120^\circ$ , the force due to the surface tension is strongly resisting the shear exerted by the surrounding fluid.

## 5. CONCLUSIONS

The effect of surface wettability on two-phase flow and dynamics of droplet pinch-off in a cross-flow microfluidic system has been studied systematically and modeled using the Navier-Stokes equation coupled with the conservative level set method. The critical physicochemical determinants varied in a wide range: capillary number,  $Ca_c < 10^{-2}$ ; the contact angle,  $120^\circ \leq \theta \leq 180^\circ$ ; flow rate ratio,  $1/10 \leq Q_r \leq 10$ . The droplet formation stages are based on the phase contours characterized as initial, filling, squeezing, pinch-off, and stable droplet. The time required for each stage of the droplet formation is a complex function of the flow rate ratio, contact angle, and capillary number. Comparison of the filling and pinch-off time based on the phase and pressure profiles as a function of the contact angle provided a new insight that the droplet pinch-off mechanism can be explained by installing the pressure sensors in the microchannels. Instantaneous interface profiles have been captured microscopically and analyzed in-depth to elucidate the droplet dynamics further. Under the hydrophobic conditions the ( $120^\circ \leq \theta \leq 150^\circ$ ), the interface shape profile transiting from

convex into concave immediately and slowly for the superhydrophobic conditions ( $150^\circ < \theta \leq 180^\circ$ ). The pressure profiles in the continuous and dispersed phases have been compared. The pressure in the dispersed phase shows an oscillating behavior and evolution as anti phase with the pressure in the continuous phase. Maximum pressure in the continuous phase is a complex function of the dimensionless parameters. The Laplace pressure acting on the interface is quantitatively higher for the hydrophobic conditions, and hence the interface adopts a flattened shape. However, the interface adopts a more curved shape due to the higher Laplace pressure for superhydrophobic conditions. The interface neck width increases in the filling stage up to a threshold value and then decreases until the pinch-off point. A similar trend is observed for all contact angles qualitatively; however, it differed quantitatively. The maximum value of the neck width is a complex function of the flow rate ratio, contact angle, and capillary number. The insights obtained from the present study would guide the designing of the microfluidic devices dispensing droplets.

## **DECLARATION OF COMPETING INTEREST**

The authors declare that they have no known competing financial interests or personal relationships that could have appeared to influence the work reported in this paper.

## **ACKNOWLEDGMENTS**

R.P. Bharti would like to acknowledge Science and Engineering Research Board (SERB), Department of Science and Technology (DST), Government of India (GoI) for providence of MATRICS grant (File No. MTR/2019/001598).

## **NOMENCLATURE**



$2r$	neck width, -
$Ca_c$	capillary number for CP (Eq. 8), -
<b>D</b>	rate of strain tensor (Eq. 3), $s^{-1}$
$h_{max}$	maximum size of mesh element, $\mu m$
$L_d$	downstream length of the main channel, $\mu m$
$L_m$	length of the main channel, $\mu m$
$L_s$	length of the side channel, $\mu m$
$L_u$	upstream length of the main channel, $\mu m$
$N_e$	total number of mesh elements, -
$p$	pressure, Pa
$p_{cp}$	pressure in CP at point 'cp', -
$p_{dp}$	pressure in DP at point 'dp', -
$p_L$	Laplace pressure, -
$Q_c$	flow rate of CP, $m^3/s$
$Q_d$	flow rate of DP, $m^3/s$
$Q_r$	flow rate ratio (Eq. 8), -
$Re_c$	Reynolds number for CP (Eq. 8), -
$t$	time, s
$t_b$	breakup (S-3) stage time, -
$t_0$	initial time, -
$t_1$	filling time, -
$t_2$	squeezing time, -
$t_3$	pinch-off time, -
$t_4$	stable droplet time, -
$t_f$	filling (S-1) stage time, -
$t_s$	squeezing (S-2) stage time, -
$t_{sd}$	stable droplet (S-4) stage time, -
<b>u</b>	velocity vector, m/s

$w_c$	width of the main channel, $\mu\text{m}$
$w_d$	width of the side channel, $\mu\text{m}$
$w_r$	channel width ratio (Eq. 8), -
$x$	stream-wise coordinate
$y$	transverse coordinate

*Dimensionless groups*

$Ca$	capillary number (Eq. 8), -
$Re$	Reynolds number (Eq. 8), -

*Greek letters*

$\beta$	slip length, $\mu\text{m}$
$\delta_{\text{avg}}$	average percent relative error, -
$\delta_{\text{max}}$	maximum percent relative error, -
$\delta_{\text{min}}$	minimum percent relative error, -
$\epsilon_s$	interface thickness controlling parameter (Eq. 6), m
$\gamma$	re-initialization or stabilization parameter (Eq. 6), m/s
$\kappa$	curvature of the interface, m
$\mu_c$	viscosity of CP, Pa.s
$\mu_d$	viscosity of DP, Pa.s
$\mu_r$	viscosity ratio (Eq. 8), -
$\phi$	level set function, dimensionless
$\rho_c$	density of CP, $\text{kg}/\text{m}^3$
$\rho_d$	density of DP, $\text{kg}/\text{m}^3$
$\rho_r$	density ratio (Eq. 8), -
$\sigma$	liquid-liquid interfacial tension, N/m
$\sigma_{\text{sl}}$	solid-liquid interfacial tension, N/m
$\sigma_{\text{sv}}$	solid-vapor interfacial tension, N/m
$\tau$	extra stress tensor (Eq. 3), $\text{N}/\text{m}^2$
$\theta$	contact angle, degrees

### *Abbreviations*

BDF	backward differentiation formula
CFD	computational fluid dynamics
CP	continuous phase
CSP	continuum surface force
DP	disperse phase
FEM	finite element method
FSI	fluid-solid interaction
LLI	liquid-liquid interface
LSM	level set method

## **REFERENCES**

- Abate, A. R., Hung, T., Sperling, R. A., Mary, P., Rotem, A., Agresti, J. J., Weiner, M. A., Weitz, D. A., 2013. DNA sequence analysis with droplet-based microfluidics. *Lab Chip* 13, 4864–4869.
- Abate, A. R., Mary, P., Van Steijn, V., Weitz, D. A., 2012. Experimental validation of plugging during drop formation in a T-junction. *Lab on a Chip* 12, 1516–1521.
- Agarwal, V. G., Singh, R., Bahga, S. S., Gupta, A., 2020. Dynamics of droplet formation and flow regime transition in a T-shaped microfluidic device with a shear-thinning continuous phase. *Physical Review Fluids* 5, 044203.
- Akhlaghi Amiri, H. A., Hamouda, A. A., 2013. Evaluation of level set and phase field methods in modeling two phase flow with viscosity contrast through dual-permeability porous medium. *International Journal of Multiphase Flow* 52, 22–34.
- Barnes, H. A., 1994. Rheology of emulsions - a review. *Colloids and Surfaces A: Physicochemical and Engineering Aspects* 91, 89–95.

- Bashir, S., Rees, J. M., Zimmerman, W. B., 2011. Simulations of microfluidic droplet formation using the two-phase level set method. *Chemical Engineering Science* 66, 4733–4741.
- Bashir, S., Rees, J. M., Zimmerman, W. B., 2014. Investigation of pressure profile evolution during confined microdroplet formation using a two-phase level set method. *International Journal of Multiphase Flow* 60, 40–49.
- Bharti, R. P., Gangawane, K. M. (Eds.), 2022. *Recent Trends in Fluid Dynamics Research. Lecture Notes in Mechanical Engineering*. Springer, Singapore.
- Boruah, M. P., Sarker, A., Randive, P. R., Pati, S., Chakraborty, S., 2018. Wettability-mediated dynamics of two-phase flow in microfluidic T-junction. *Physics of Fluids* 30 (12), 122106.
- Brackbill, J., Kothe, D., Zemach, C., 1992. A continuum method for modeling surface tension. *Journal of Computational Physics* 100, 335–354.
- Carrier, O., Funfschilling, D., Li, H. Z., 2014. Effect of the fluid injection configuration on droplet size in a microfluidic T junction. *Physical Review E* 89, 013003.
- Christopher, G. F., Noharuddin, N. N., Taylor, J. A., Anna, S. L., 2008. Experimental observations of the squeezing-to-dripping transition in T-shaped microfluidic junctions. *Physical Review E* 78, 036317.
- COMSOL, 2022. *COMSOL Multiphysics Reference Manual, version 6.0*. COMSOL, Multiphysics.  
URL [https://doc.comsol.com/6.0/doc/com.comsol.help.comsol/COMSOL\\_ReferenceManual.pdf](https://doc.comsol.com/6.0/doc/com.comsol.help.comsol/COMSOL_ReferenceManual.pdf)
- De menech, M., Garstecki, P., Jousse, F., Stone, H. A., 2008. Transition from squeezing to dripping in a microfluidic T-shaped junction. *Journal of Fluid Mechanics* 595, 141–161.
- Deka, D. K., Pati, S., Randive, P. R., 2022. Implications of capillarity-wettability interaction

- on geometrically mediated droplet splitting mechanism. *Colloids and Surfaces A: Physicochemical and Engineering Aspects* 633, 127873.
- Dhondi, P., Venkateshwarlu, A., Bharti, R. P., 2022. Effect of shear rate on non-Newtonian droplet generation in T-junction microfluidic system. In: Bharti, R. P., Gangawane, K. M. (Eds.), *Recent Trends in Fluid Dynamics Research. Lecture Notes in Mechanical Engineering*. Springer, Singapore, Ch. 13, pp. 161–172.
- Eggersdorfer, M. L., Seybold, H., Ofner, A., Weitz, D. A., Studart, A. R., 2018. Wetting controls of droplet formation in step emulsification. *Proceedings of the National Academy of Sciences* 115 (38), 9479–9484.
- Gada, V. H., Sharma, A., 2009. On derivation and physical interpretation of level set method-based equations for two-phase flow simulations. *Numerical Heat Transfer, Part B: Fundamentals* 56, 307–322.
- Garstecki, P., Fuerstman, M. J., Stone, H. A., Whitesides, G. M., 2006. Formation of droplets and bubbles in a microfluidic T-junction - Scaling and mechanism of break-up. *Lab on a Chip* 6 (3), 437–446.
- Gerbeau, J.-F., Lelièvre, T., 2009. Generalized Navier boundary condition and geometric conservation law for surface tension. *Computer Methods in Applied Mechanics and Engineering* 198 (5), 644–656.
- Glawdel, T., Elbuken, C., Ren, C. L., 2012. Droplet formation in microfluidic T-junction generators operating in the transitional regime. I. Experimental observations. *Physical Review E* 85, 016322.
- Gupta, A., Murshed, S. M., Kumar, R., 2009. Droplet formation and stability of flows in a microfluidic T-junction. *Applied Physics Letters* 94.

- Hernández-Cid, D., Pérez-González, V., Gallo-Villanueva, R., González-Valdez, J., Mata-Gómez, M., 2022. Modeling droplet formation in microfluidic flow-focusing devices using the two-phases level set method. *Materials Today : Proceedings* 48, 30–40.
- Hou, X., Zhang, Y., Trujillo-de Santiago, G., Alvarez, M., Ribas, J., Jonas, S., Weiss, P., Andrews, A., Aizenberg, J., Khademhosseini, A., 2017. Interplay between materials and microfluidics. *Nature Reviews Materials* 2 (5), 17016.
- Huhtamaki, T., Tian, X., Korhonen, J. T., Ras, R. H. A., 2018. Surface-wetting characterization using contact-angle measurements. *Nature Protocols* 13, 1521 – 1538.
- Jung, S. H., Bulut, S., Busca Guerzoni, L., Günther, D., Braun, S., De Laporte, L., Pich, A., 2022. Fabrication of pH-degradable supramacromolecular microgels with tunable size and shape via droplet-based microfluidics. *Journal of Colloid and Interface Science* 617, 409–421.
- Kaminski, T. S., Garstecki, P., 2017. Controlled droplet microfluidic systems for multistep chemical and biological assays. *Chemical Society Reviews* 46, 6210–6226.
- Kawakatsu, T., Trägårdh, G., Trägårdh, C., Nakajima, M., Oda, N., Yonemoto, T., 2001. The effect of the hydrophobicity of microchannels and components in water and oil phases on droplet formation in microchannel water-in-oil emulsification. *Colloids and Surfaces A: Physicochemical and Engineering Aspects* 179 (1), 29–37.
- Law, K.-Y., 2014. Definitions for hydrophilicity, hydrophobicity, and superhydrophobicity: getting the basics right. *Journal of Physical Chemistry Letters* 5 (4), 686–688.
- Maan, A. A., Sahin, S., Mujawar, L. H., Boom, R., Schroën, K., 2013. Effect of surface wettability on microfluidic EDGE emulsification. *Journal of Colloid and Interface Science* 403, 157–159.

- Mastiani, M., Seo, S., Jimenez, S. M., Petrozzi, N., Kim, M. M., 2017. Flow regime mapping of aqueous two-phase system droplets in flow-focusing geometries. *Colloids and Surfaces A: Physicochemical and Engineering Aspects* 531, 111–120.
- Mirzaaghaian, A., Ramiar, A., Ranjbar, A. A., Warkiani, M. E., 2020. Application of level-set method in simulation of normal and cancer cells deformability within a microfluidic device. *Journal of Biomechanics* 112, 110066.
- Moon, S.-K., Cheong, I. W., Choi, S.-W., 2014. Effect of flow rates of the continuous phase on droplet size in dripping and jetting regimes in a simple fluidic device for coaxial flow. *Colloids and Surfaces A: Physicochemical and Engineering Aspects* 454, 84–88.
- Nisisako, T., Torii, T., Higuchi, T., 2002. Droplet formation in a microchannel network. *Lab on a Chip* 2, 24–26.
- Olsson, E., Kreiss, G., 2005. A conservative level set method for two phase flow. *Journal of Computational Physics* 210, 225–246.
- Osher, S., Sethian, J. A., 1988. Fronts propagating with curvature-dependent speed: Algorithms based on Hamilton-Jacobi formulations. *Journal of Computational Physics* 79, 12–49.
- Samadder, S., Venkateshwarlu, A., Bharti, R. P., 2022. Effects of inertial force and interfacial tension on droplet generation in a T-junction microfluidic system. In: Bharti, R. P., Gangawane, K. M. (Eds.), *Recent Trends in Fluid Dynamics Research. Lecture Notes in Mechanical Engineering*. Springer, Singapore, Ch. 14, pp. 173–182.
- Schroen, K., Berton-Carabin, C., Renard, D., Marquis, M., Boire, A., Cochereau, R., Amine, C., Marze, S., 2021. Droplet microfluidics for food and nutrition applications. *Micromachines* 12 (8), 863.

- Shi, Y., Tang, G. H., Xia, H. H., 2014. Lattice Boltzmann simulation of droplet formation in T-junction and flow focusing devices. *Computers and Fluids* 90, 155–163.
- Thorsen, T., Roberts, R. W., Arnold, F. H., Quake, S. R., 2001. Dynamic pattern formation in a vesicle-generating microfluidic device. *Physical Review Letters* 86, 4163–4166.
- Trefethen, L., 1969. *Surface Tension in Fluid Mechanics*, National Committee for Fluid Mechanics Films, MIT.
- van der Graaf, S., Nisisako, T., G. P. H. Schroën, C., G. M. van der Sman, R., M. Boom, R., 2006. Lattice Boltzmann Simulations of Droplet Formation in a T-Shaped Microchannel. *Langmuir* 22, 4144–4152.
- van Steijn, V., Kleijn, C. R., Kreutzer, M. T., 2009. Flows around confined bubbles and their importance in triggering pinch-off. *Physical Review Letters* 103, 214501.
- van Steijn, V., Kleijn, C. R., Kreutzer, M. T., 2010. Predictive model for the size of bubbles and droplets created in microfluidic T-junctions. *Lab on a Chip* 10, 2513–2518.
- van Steijn, V., Kreutzer, M. T., Kleijn, C. R., 2007.  $\mu$ -PIV study of the formation of segmented flow in microfluidic T-junctions. *Chemical Engineering Science* 62, 7505–7514.
- Venkateshwarlu, A., Bharti, R. P., 2021. Effects of capillary number and flow rate on the hydrodynamics of droplet generation in two-phase cross-flow microfluidic systems. *Journal of Taiwan Institute of Chemical Engineers* 129, 64–79.
- Venkateshwarlu, A., Bharti, R. P., 2022a. Effect of contact angle on droplet generation in a T-junction microfluidic system. In: Bharti, R. P., Gangawane, K. M. (Eds.), *Recent Trends in Fluid Dynamics Research. Lecture Notes in Mechanical Engineering*. Springer, Singapore, Ch. 11, pp. 137–147.
- Venkateshwarlu, A., Bharti, R. P., 2022b. Interface evolution and pinch-off mechanism



of droplet in two-phase liquid flow through T-junction microfluidic system. *Colloids and Surfaces A: Physicochemical and Engineering Aspects* 642, 128536.

Wang, S., Yang, X., Wu, F., Min, L., Chen, X., Hou, X., 2020. Inner Surface Design of Functional Microchannels for Microscale Flow Control. *Small* 16 (9), 1–18.

Weng, L., Spoonamore, J. E., 2019. Droplet Microfluidics-Enabled High-Throughput Screening for Protein Engineering. *Micromachines* 10 (11), 734.

Wong, V. L., Loizou, K., Lau, P. L., Graham, R. S., Hewakandamby, B. N., 2017. Numerical studies of shear-thinning droplet formation in a microfluidic T-junction using two-phase level-SET method. *Chemical Engineering Science* 174, 157–173.

Wu, J., Kodzius, R., Cao, W., Wen, W., 2014. Extraction, amplification and detection of DNA in microfluidic chip-based assays. *Microchimica Acta* 181 (13-14), 1611–1631.

Yan, Y., Guo, D., Wen, S. Z., 2012. Numerical simulation of junction point pressure during droplet formation in a microfluidic T-junction. *Chemical Engineering Science* 84, 591–601.